Contribution of water-leaving radiances to multiangle, multispectral polarimetric observations over the open ocean: bio-optical model results for case 1 waters

Jacek Chowdhary, Brian Cairns, and Larry D. Travis

Multiangle, multispectral photopolarimetry of atmosphere–ocean systems provides the fullest set of remote sensing information possible on the scattering properties of aerosols and on the color of the ocean. Recent studies have shown that inverting such data allows for the potential of separating the retrieval of aerosol properties from ocean color monitoring in the visible part of the spectrum. However, the data in these studies were limited to those principal plane observations where the polarization of water-leaving radiances could be ignored. Examining similar potentials for off-principal plane observations requires the ability to assess realistic variations in both the reflectance for and bidirectionality of polarized water-leaving radiances for such viewing geometries. We provide hydrosol models for use in underwater light scattering computations to study such variations. The model consists of two components whose refractive indices resemble those of detritus–minerallike and planktonlike particles, whose size distributions are constrained by underwater light linear polarization signatures, and whose mixing ratios change as a function of particulate backscattering efficiency. Multiple scattering computations show that these models are capable of reproducing realistic underwater light albedos for wavelengths ranging from 400 to 600 nm, and for chlorophyll *a* concentrations ranging from 0.03 to 3.0 mg/m^3. Numerical results for spaceborne observations of the reflectance for total and polarized water-leaving radiances are provided as a function of polar angles, and the change in these reflectances with wavelength, chlorophyll *a* concentration, and hydrosol model are discussed in detail for case 1 (open ocean) waters.

OCIS codes: 010.0010, 280.0280, 290.4210, 290.5850.

1. Introduction

The linear polarization of light observed over the ocean from an aircraft or spacecraft contains a wealth of information that is not readily available from total radiance data. Light, in its most general form, can be described as the sum of an unpolarized component and a fully polarized component.[1] Linearly polarized light makes up most of the latter component (with typically only a very tiny fraction of circular polarized light), and originates in atmosphere–ocean systems from particle scattering in the atmosphere and ocean, from skylight reflection by the ocean surface, and from transmission of light by the ocean surface. Both the total and polarized radiance exhibit features as a function of scattering angle and wavelength that can be used to extract information about the atmosphere and the ocean. However, the polarized radiance features are generally much sharper, more numerous, and show larger variations than the total radiance features because of their large sensitivity to aerosol properties and weak sensitivity to multiple scattering. To match such polarimetric variations requires the use of sophisticated numerical techniques to model the scattering properties of complicated aerosol particles[2]; however, they also allow these properties to be retrieved with accuracies far exceeding those of photometric retrievals.[3,4] Examples of such retrieval differences are given by Chowdhary *et al.*[5] and Gérard *et al.*[6] for observations in the near infrared, where one can neglect the contribution of water-leaving radiances. The situation becomes more complex for visible wavelengths, where one must ac-

J. Chowdhary (jchowdhary@giss.nasa.gov) and B. Cairns are with the Department of Applied Physics and Applied Mathematics, Columbia University, 2880 Broadway, New York, New York 10025 and NASA Goddard Institute of Space Studies, 2880 Broadway, New York, New York 1025. L. D. Travis is with NASA Goddard Institute of Space Studies, 2880 Broadway, New York, New York 10025.

Received 4 November 2005; revised 31 March 2006; accepted 5 April 2006; posted 6 April 2006 (Doc. ID 65639).

0003-6935/06/225542-26$15.00/0

count for light emerging from the ocean body. The radiance of this light contributes less than 20% of the total observed from space, but its absolute magnitude varies substantially with the amount of phytoplankton.[7,8] This makes it extremely difficult to retrieve the properties of aerosol particles and especially of ocean bodies from photometric measurements at such wavelengths. Commonly, one incorporates the infrared measurements to constrain the amount of atmospheric scattering in the visible,[9] but such extrapolations still require assumptions on the spectral behavior of aerosol optical properties.

In a recent paper[10] we explored inverting visible polarized radiances obtained over the ocean by the Research Scanning Polarimeter (RSP) instrument,[11] an airborne version that is functionally similar to the Aerosol Polarimetry Sensor (APS).[12] Using for the computation of underwater light contribution a hydrosol model whose scattering function resembled the ones measured by Petzold[13] for turbid waters, we showed that the polarized contribution of this light to our data set was negligibly small. This important observation enabled us to expand the range of wavelengths used for aerosol retrieval and to obtain additional valuable information of aerosol refractive indices in the visible part of the spectrum. Similar conclusions were reached by Chami *et al.*,[14] who employed a phytoplankton model for their underwater light scattering computations. However, it has been known in the ocean color monitoring community that phytoplankton alone cannot provide the amount of backscattering necessary to produce observed ocean albedos,[15] and that the use of Petzold's scattering functions can lead to uncomfortably high ocean albedos.[16] This does not much affect the conclusions drawn by Chami *et al.*[14] and by Chowdhary *et al.*[10] since both analyses were confined to the observations in the principal plane where the polarization of water-leaving radiances is inherently small near the backscattering direction, and relatively small for forward-scattering directions coinciding with the sunglint region. But expanding such studies to include sideward-scattering directions and/or total radiances require hydrosol models that lead to more realistic ocean albedos, especially if the results are going to be used for quantitative analyses of actual remote sensing data.

Unfortunately, only few measurements of angular scattering by hydrosols have been reported thus far (Volten *et al.*[17] and references therein). While these measurements can be reproduced fairly well by Mie computations,[18,19] they provide insufficient data on the change in backscattering efficiency with phytoplankton concentrations.[20] The existence of such changes has been derived from theoretical considerations and underwater light measurements, and is routinely used to explain ocean color variations.[8] It has been approximated by variations in particle size distribution[21] and/or the refractive index[22] of hydrosols, but data to substantiate such relationships are even scarcer. Most radiative transfer studies of underwater light up to the present have thus focused on sensitivity analyses rather than remote sensing applications; i.e., hydrosol properties and/or turbidity were simply varied within acceptable boundaries to examine their relative effects on fluxes,[23–25] total radiance distributions,[26,27] and polarized radiance distributions[28,29] in atmosphere–ocean systems. Some studies adopted elaborate hydrosol models consisting of 5+ microbial species to study variations in the inherent optical properties of ocean bodies and their impact on remotely sensed reflectances[30,31]; however, the complexity of such models (including the large number of free parameters) is difficult to implement for use in remote sensing. Ocean properties relevant to the determination of ocean color can, on the other hand, be retrieved without precise knowledge of the hydrosol scattering function by measuring ratios of upwelling to downwelling underwater light irradiances.[32,33] Nevertheless, the need for hydrosol scattering functions that are more realistic than those used by Chami *et al.*[14] and by Chowdhary *et al.*[10] has also been expressed in ocean color retrieval studies; in particular those that examine approximations made for the bidirectionality of water-leaving radiances.[34–36]

In this study, we seek to perform vector radiative transfer computations of underwater light whose scattering properties *and* ocean body albedo are consistent with ocean color statistics, such that the resulting water-leaving radiances can be used to study the separation of aerosol retrieval and ocean color monitoring in polarimetric remote sensing observations. We develop for this purpose a hydrosol model consisting of two components whose particle properties are constrained by maximum underwater light polarization signatures, and whose mixing ratios are determined by the backscattering efficiency predicted by ocean color algorithms. The ocean color algorithms are for case 1 waters, i.e., waters whose optical properties are dominated by living organisms and their associated by-products.[37] According to Morel,[8] more than 98% of the world's ocean can be classified as such. We show that the resulting hydrosol scattering functions lead to ocean albedos that are in excellent agreement with predictions made for visible wavelengths and a wide range of ocean biomass concentrations (oligotrophic to moderately eutrophic waters) when combined with bio-optical relations for the scattering and absorption coefficients. Our results are not unique, i.e., we provide multiple solutions of our model that lead to the same ocean albedos and color variations. However, the purpose of this study is not to derive hydrosol properties, but to provide a simple radiative transfer model for underwater light scattering that allows for the study of total and polarized radiance distributions emerging from ocean bodies with realistic albedos and ocean colors, as might actually be observed from an aircraft or spacecraft. To address differences that might arise from assumptions made in the course of our model derivation, we compare water-leaving radiance distributions obtained from a solution of our model with those obtained from a hydrosol model whose single scattering radiance and polarization properties resemble extreme observations.

The two-component hydrosol model approach to reconcile underwater light scattering computations with ocean color statistics has been suggested before. For example, Gordon[20] concludes that in order to reproduce the change in backscattering efficiency with phytoplankton concentration, one must accept at least two particulate components for hydrosol scattering. He defined these components as detritus and phytoplankton, and adopted for their scattering functions the original measurements by Petzold[13] and a modified version, respectively. Haltrin[38,39] on the other hand provides the parameterization of a two-component hydrosol scattering function and a two-term Henyey–Greenstein scattering function, respectively, based on extensive measurements taken by a number of researchers. Both Gordon[20] and Haltrin[38] force their models to agree with ocean colors statistics by tuning their mixing ratios. However, their scattering functions are given in analytical formats rather than Mie solutions, which makes it impossible to extend their results to include polarization. Twardowski *et al.*[22] use altogether a different approach in which the refractive index and size distribution of a one-component hydrosol model are varied to fit observed backscattering efficiencies and attenuation coefficient spectra, respectively. Mobley *et al.*[40] use a similar approach except for postulating a relationship between particle refractive index and size distribution. Both their models can be used to compute polarization properties of hydrosols, but we found the resulting values to be much higher than suggested by underwater light polarization measurements [e.g., see Fig. 3(b) and related discussion in Subsection 3.A]. Furthermore, their models imply the use of a hydrosol model whose microphysical properties vary continuously with phytoplankton concentration, which is more cumbersome to employ for operational purposes than the use of two hydrosol components whose mixing rations are varied continuously. Finally, the approach followed by Mehrtens and Martin[41] and by Morel *et al.*[42] is quite similar to the one presented in this work: Marine particulates are decomposed into two components, the scattering properties of each of which are defined by a set of particle refractive index and size distribution parameters, and the mixing of which leads to realistic ocean color variations. Both their models address, therefore, the need expressed by Morel and Gentili[34–36] for more realistic hydrosol scattering functions. However, the set of parameters chosen for each hydrosol component in these models is not constrained by polarization measurements. Consequently, their mixtures lead to underwater light polarization that is not necessarily consistent with such measurements. Furthermore, they do not discuss uncertainties associated with the nonuniqueness problem of viable hydrosol models.

2. Theory

A. Basic Radiative Transfer Concepts

Consider first the occurrence of unidirectional light in a plane-parallel atmosphere–ocean system (AOS). Let the direction of light propagation be denoted by the real unit vector **k**. To describe the geometry of light propagation, we use a right-handed Cartesian coordinate system with the positive z coordinate measuring height from the ocean surface (Fig. 1). Then **k** can be specified by the coordinates (u, φ), where $u = -\cos\theta$, θ is the zenith angle measured from the positive z axis, and φ is the azimuth angle measured in the clockwise direction from the positive x axis when looking upward (see Appendix A for notations). Note that $u < 0$ for upwelling radiation while $u > 0$ for downwelling radiation. For future use, we also define $\mu = |u|$. The intensity and state of polarization of light traveling in the direction **k** can be described by the (4×1) Stokes vector **I** given by

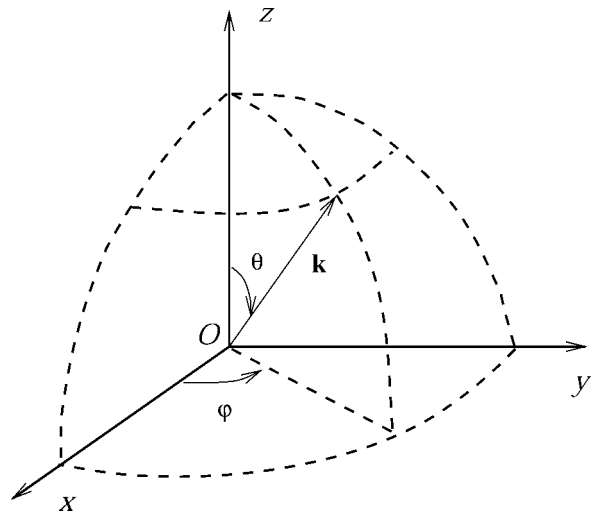

Fig. 1. Local geometry of light traveling through O in the direction of **k**, where **k** is a unit vector specified by the polar angles (θ, φ).

$$\mathbf{I} = \begin{bmatrix} I \\ Q \\ U \\ V \end{bmatrix}, \tag{1}$$

which has as its components the Stokes parameters I, Q, U, and V. Stokes parameter I is equal, apart from a constant, to the net monochromatic energy flux ($\mathrm{W\,m^{-2}\,nm^{-1}}$). Stokes parameters Q and U describe the linearly polarized component of this flux, while its circular polarized component is described through Stokes parameter V. We define further the linear polarized component of I as

$$P = \sqrt{Q^2 + U^2}. \tag{2}$$

A more detailed discussion on the Stokes parameters I, Q, U, V, and on the direction of polarization for P is provided by Hovenier and van der Mee.[43] Multiple scattering by randomly distributed particles causes the field of light to depend also on the direction and size of solid angle considered. The quantity that takes these properties into account, and which is also appropriate for use in radiative transfer computations,

is the (4×1) so-called specific intensity or radiance vector $\tilde{\mathbf{I}}$. We refer to Mishchenko[44] for a thorough discussion on the specific intensity vector and its relation to the Stokes vector. We use a tilde to identify the radiance equivalents of I, Q, U, V, and P. That is, $\tilde{I}$ is the first parameter of the specific intensity vector $\tilde{\mathbf{I}}$ and is equal to the total radiance (W m^{-2} nm^{-1} sterad^{-1}) of a beam of light, for example.

Consider now a small-volume element dV of the atmosphere or ocean body containing randomly oriented particles. To locate the volume element we define its optical depth τ as in Hansen and Travis:[1] We assume that each scattering process in dv occurs independently of the others, which requires that the particle centers are separated by at least four times their radius.[45] Also, we ignore internal emission sources. Let $\tilde{\mathbf{I}}(\tau, u, \varphi)$ denote the specific intensity vector of a quasi-monochromatic beam of light illuminating dv in the direction of $\mathbf{k}$ given by (u, φ), and $d\tilde{\mathbf{I}}(\tau, u', \varphi')$ the specific intensity vector of the fraction of light emerging from dv in the direction of $\mathbf{k}'$ given by (u', φ'). Choosing the meridional plane (i.e., plane containing the direction of light propagation and the z axis) as a reference plane for intensity vectors, one can describe the transfer of polarized light in our plane-parallel atmosphere–ocean system by

$$u' d\tilde{\mathbf{I}}(\tau', u', \varphi') = -\tilde{\mathbf{I}}(\tau, u', \varphi') d\tau + \frac{\omega}{4\pi} \int_{-1}^{1} u du \times \int_{0}^{2\pi} d\varphi \mathbf{Z}(u', \varphi'; u, \varphi) \times \tilde{\mathbf{I}}(\tau, u, \varphi) d\tau, \quad (3)$$

where $d\tau$ and ω are the optical thickness and single scattering albedo of dv, respectively, and $\mathbf{Z}$ is the (4×4) phase matrix given by

$$\mathbf{Z}(u', \varphi'; u, \varphi) = \mathbf{L}(\pi - i_2)\mathbf{F}(\Theta)\mathbf{L}(-i_1). \quad (4)$$

In Eq. (4), $\mathbf{F}$ is the scattering matrix of dv and depends only on the so-called scattering angle Θ between (u, φ) and (u', φ') because it assumes the scattering plane (plane through $\mathbf{k}$ and $\mathbf{k}'$) as the reference plane for $\tilde{\mathbf{I}}(\tau, u, \varphi)$ and $\tilde{\mathbf{I}}(\tau, u', \varphi')$. Matrices $\mathbf{L}(-i_1)$ and $\mathbf{L}(\pi - i_2)$ describe the transformation of $\tilde{\mathbf{I}}(\tau, u, \varphi)$ and $\tilde{\mathbf{I}}(\tau, u', \varphi')$ when rotating their reference planes to and from the scattering planes, respectively, and are provided by Hovenier and van der Mee.[43] If each of the particles in dv can be characterized by a plane of symmetry (e.g., homogeneous spheres and spheroids), or if it is accompanied in dv by a mirror particle, then $\mathbf{F}$ takes the form[46]

$$\mathbf{F}(\Theta) = \begin{bmatrix} a_1(\Theta) & b_1(\Theta) & 0 & 0 \\ b_1(\Theta) & a_2(\Theta) & 0 & 0 \\ 0 & 0 & a_3(\Theta) & 0 \\ 0 & 0 & 0 & a_4(\Theta) \end{bmatrix}, \quad (5)$$

where a_1 is just equal to the scattering function of dv. We omit the bold font face of $\mathbf{F}$ when referring to its scattering function, i.e., $F \equiv a_1$, and normalize it according to Hansen and Travis[1]:

$$\int_{4\pi} F(\Theta) \frac{d\Omega}{4\pi} = 1, \quad (6)$$

where $d\Omega$ is the volume element of the solid angle (sterad). Note that this normalization differs by a factor of $(4\pi)^{-1}$ from the normalization commonly adopted by the ocean color community (e.g., Gordon[47]). In addition, it is customary to use $-F_{21}/F_{11}$ (%) for the degree of linear polarization of light singly scattered by dv when illuminated by a unidirectional beam of unpolarized light.

B. Bio-Optical Equations for Case 1 Waters

To describe the color of the bulk ocean, it is convenient to approximate the reflection properties of the ocean body by a Lambertian reflector whose albedo A_{blk} varies with the wavelength λ(nm). Albedo A_{blk} is then equal to the ratio of the upwelling irradiance E_u to downwelling irradiance E_d just below the ocean surface, i.e.,

$$A_{\text{blk}}(\lambda) = \frac{E_u(\lambda)}{E_d(\lambda)}, \quad (7)$$

which is independent of instrumental calibration and can therefore be measured relatively easy. Note however that E_d and E_u vary with the sun angle and ocean properties, respectively. Morel and Prieur[37] show that A_{blk} can be expressed in terms of the backscattering coefficient $s_{\text{blk}}(\text{m}^{-1})$ and absorption coefficient $a_{\text{blk}}(\text{m}^{-1})$ of bulk oceanic water according to

$$A_{\text{blk}}(\lambda) = \alpha \frac{s_{\text{blk}}(\lambda)}{a_{\text{blk}}(\lambda)}, \quad (8)$$

where α is about 0.3 for oligotrophic waters and clear skies with the sun overhead. Variations of the factor α with decreasing solar zenith angles and increasing biomass concentrations are given by Morel and Gentili[34] and by Morel *et al.*[42] The bulk backscattering coefficient s_{blk} in Eq. (8) can be written as[8]

$$s_{\text{blk}}(\lambda) = 0.5 b_w(\lambda) + q_p(\lambda) b_p(\lambda = 550), \quad (9)$$

where b_w and b_p are the scattering coefficients (m^{-1}) of the pure water and particulate components of the ocean, respectively, and q_p is the backscattering efficiency of the particulate scattering function F_p, i.e.,

$$q_p(\lambda) = 2\pi \int_{\pi/2}^{\pi} \frac{F_p(\Theta, \lambda)}{4\pi} \sin(\Theta) d\Theta, \quad (10)$$

where the factor of $(4\pi)^{-1}$ derives from the normalization of $F_p(\Theta)$ in Eq. (6).

In situ measurements have shown b_p to be systematically correlated with [Chl], the concentration (mg m^{-3}) of chlorophyll *a*, in case 1 waters. Chlorophyll *a* is a photosynthetic pigment found in microscopic plants and phytoplankton that absorbs strongly in the blue part of the spectrum. Hence [Chl] affects the color of the ocean and can also be used as a proxy for the amount of phytoplankton biomass. Its magnitude varies from 0.01 mg m^{-3} for oligotrophic oceans to over 10 mg m^{-3} for strongly eutrophic oceans, but is, according to Morel and Gentili,[34] for most open oceans smaller than 1 mg m^{-3}. Following Morel and Maritorena,[16] we use for b_p:

$$b_p(\lambda) = b_p^{0}[\mathrm{Chl}]^{0.766}\,(550/\lambda), \quad b_p^{0} = 0.416, \quad (11)$$

where the dependence on [Chl] of b_p on the left-hand side is implicitly assumed. We adopt this convention for all parameters relating to particulate matter in the present work. The nonlinear relationship between b_p and [Chl] in Eq. (11) can be attributed to the relative increase in amount of nonchlorophyllic particles (e.g., detritus) with decreasing [Chl].[48] The accompanied change in hydrosol scattering function is thought to be the source for the variation in the backscattering efficiency q_p derived from ocean color observations. Morel[8] parameterized this variation as a function of λ and [Chl] based on theoretical considerations and *in situ* measurements. We use the modified version of this parameterization given by Morel and Maritorena,[16] which reads as

$$q_p(\lambda) = 0.002 + 0.01\{0.50 - 0.25\log_{10}[\mathrm{Chl}]\} \times (\lambda/550)^{k}, \quad (12)$$

where

$$k = \begin{cases} 0.5(\log_{10}[\mathrm{Chl}] - 0.3), & 0.02 \le [\mathrm{Chl}] \le 2 \text{ mg m}^{-3} \\ 0, & \text{otherwise.} \end{cases} \quad (13)$$

The variation of absorption coefficient a_{blk} with λ and [Chl] has been studied by Bricaud *et al.*[49] for suspended particulate matter. They found similar nonlinear relationships with [Chl] as in Eq. (11) for both phytoplankton and nonalgal particles, with the value of the exponent depending on λ.[50] However, as pointed out by Morel and Maritorena,[16] such measurements do not account for absorption by colored dissolved organic matter (CDOM, or "yellow substance"), which can be substantial in the blue. Instead, we retrieve a_{blk} and A_{blk} simultaneously by solving Eq. (8) together with

$$a_{\mathrm{blk}}(\lambda) = K_{\mathrm{blk}}(\lambda)\{1 - A_{\mathrm{blk}}(\lambda)\}\,\frac{\mu_d\mu_u}{\mu_d A_{\mathrm{blk}}(\lambda) + \mu_u}, \quad (14)$$

where μ_d and μ_u are the average cosine directions with respect to the vertical for the downward and upward underwater light flux, respectively, and

$$K_{\mathrm{blk}}(\lambda) = K_w(\lambda) + K_{\mathrm{bio}}(\lambda) \quad (15)$$

is the attenuation coefficient (m^{-1}) for downward irradiance with

$$K_w(\lambda) = a_w(\lambda) + 0.5b_w(\lambda) \quad (16)$$

and

$$K_{\mathrm{bio}}(\lambda) = \chi(\lambda)[\mathrm{Chl}]^{e(\lambda)}. \quad (17)$$

In Eqs. (16) and (17), a_w is the absorption coefficient (m^{-1}) for pure seawater, and $\chi(\lambda)$ and $e(\lambda)$ are the coefficients tabulated by Morel and Maritorena[16] to fit observed spectra of the attenuation coefficient K_{bio} of all biogenic matter (particulate and dissolved). Equation (14) is an exact relationship derived from Gershun's divergence law for irradiance in which the change of A_{blk} with depth is neglected (Prieur and Sathyendranath[51]). It has the advantage of relating a_{blk} to *in situ* measurements of K_{bio} and thus incorporates absorption by all materials present, including yellow substance. Note that substituting Eq. (8) for A_{blk} in Eq. (14) leads to a second-order polynomial expression for a_{blk}, which can be handled analytically instead of using the iterative method proposed by Morel.[8] We solve this equation as a function of λ and [Chl] using for μ_d and μ_u the values provided by Morel and Maritorena.[16] The coefficients b_w and a_w in Eqs. (9) and (16) for seawater are taken from Smith and Baker[52] and from Pope and Fry,[53] respectively.

C. Single Scattering Properties for Case 1 Waters

The bio-optical model described in Subsection 2.B implies that, from an optical standpoint, one can treat the bulk ocean of case 1 waters as a mixture of pure seawater and a particulate component with scattering properties (b_w, a_w) and $(b_p, a_{\mathrm{blk}} - a_w, q_p)$, respectively. The bulk scattering matrix and single scattering albedo for such mixtures are given by

$$\mathbf{F}_{\mathrm{blk}}(\Theta, \lambda) = \frac{b_w(\lambda)\mathbf{F}_w(\Theta, \lambda) + b_p(\lambda)\mathbf{F}_p(\Theta, \lambda)}{b_w(\lambda) + b_p(\lambda)}, \quad (18)$$

$$\omega_{\mathrm{blk}}(\lambda) = \frac{b_w(\lambda) + b_p(\lambda)}{b_w(\lambda) + b_p(\lambda) + a_{\mathrm{blk}}(\lambda)}, \quad (19)$$

respectively, where $\mathbf{F}_w$ is the scattering matrix of pure seawater. Measurements performed by Morel[54] show that $\mathbf{F}_w$ can be approximated by Rayleigh scattering with a depolarization factor δ_w of 0.09. Hence to solve the equation of transfer for case 1 waters requires finding appropriate models for $\mathbf{F}_p$ whose scattering function satisfies Eqs. (10), (12), and (13).

There are many sources of elastic scattering that can contribute to $\mathbf{F}_p$ such as scattering by inorganic

and organic particles, which include living (bacterioplankton, phytoplankton, and zooplankton) and nonliving varieties, and even by air bubbles.[15,55] The angular features of these scattering contributions are determined by the size, shape, and composition of their scattering sources. The magnitudes of these scattering contributions depend in addition on the abundance of their scattering sources. In what follows, we assume the shape of each scattering source to be spherical, and the composition of each scattering source to be represented by a single value of refractive index. Both assumptions are generally not true, e.g., phytoplankton exhibit a wide variety of shapes[17,56] and are often heterogeneous.[57,58] However, they allow the scattering properties of these particles to be computed from the Mie theory, which is relatively simple to use and requires only the size distribution and refractive index as input parameters. While it is becoming possible to compute the scattering properties of complex nonspherical particles,[59] there is simply not enough information available on the detailed structure of marine particles to compile representative cases. Furthermore, laboratory measurements show that while the shapes of phytoplankton scattering functions are sensitive to particle inclusions such as gas vacuoles, they show mainly changes in the forward-scattering hemisphere.[17] These measurements suggest that the internal variation of phytoplankton particles may have a bigger impact on the backscattering efficiency[60] q_p than on the distribution of radiance reflected in the backscattering hemisphere. We will account for the former impact by fitting q_p in our hydrosol models to the semiempirical variations with [Chl] given by Eq. (12). Furthermore, Mueller matrix measurements performed for various oceans[61] and phytoplankton cultures[62] show linear polarization signatures that can be reproduced from scattering by homogeneous spheres (Fig. 1 in Kouzoubov *et al.*[63]) even though differences were observed for the diagonal elements a_2, a_3, and a_4 of the scattering matrix. Nevertheless, theoretical computations show that internal structures such as spherical layers can change the shape of scattering functions for sideward and backward directions.[58] And nonspherical shapes have been used to modify the backscattering lobes of these functions.[42] We will address the significance of ignoring such effects by comparing our results with those obtained for highly refractive spheres which exhibit more pronounced backscattering lobes.

Both the equation of transfer given by Eq. (3) and the bio-optical model presented in Eqs. (8)–(17) ignore inelastic scattering processes such as Raman scattering and fluorescence. Fluorescence by chlorophyll *a* leads to a distinctive peak in A_{blk} at $\lambda = 685$ nm,[64] which can be avoided by limiting our analyses to $\lambda \leq 600$ nm. Yellow substance fluorescence can also contribute to A_{blk} in the blue–green but its magnitude becomes only important in coastal regions influenced by terrestrial dissolved organic matter (DOM) discharge,[65] i.e., in case 2 waters.[37] Raman scattering, on the other hand, can contribute significantly (15%–20%) to the water-leaving radiance for $\lambda \geq 520$ nm and $0.05 \leq [\mathrm{Chl}] \leq 0.1$ mg m^{-3}.[66] Fortunately, the bio-optical model is capable of reproducing measurements of A_{blk} (which *include* Raman scattering contributions) quite well for green light and small [Chl]. Morel and Maritorena[16] argue that this should not be surprising given the statistical nature of the bio-optical equations and the span of A_{blk} values with λ. Indeed, we shall see that A_{blk} can vary with [Chl] by several factors, i.e., much larger than the contribution of Raman scattering for given [Chl]. Simulations performed by Morel *et al.*[42] show further that ignoring Raman scattering in underwater light scattering computations does not notably change the angular distribution of upwelling light. We conclude that the uncertainty in F_{blk} due Raman scattering can be ignored in the present work. The corresponding uncertainties in the polarized radiance of scattered light are not addressed, but are assumed to be small because they originate from a fixed percentage of F_{blk}.

The variation of q_p with [Chl] implies that there are at least two types of particulates present in case 1 waters whose scattering matrices $\mathbf{F}_{\mathrm{hyd}}$ contribute to $\mathbf{F}_p$ and whose relative abundance varies with [Chl]. While q_p is likely to originate from scattering by many more classes of marine particulates,[55] it is convenient to use only two effective particulate components given the limited understanding on the scattering contributions of each such class and the increase in hydrosol model complexity with number of classes. To obtain the scattering properties of two such components, we take note of the following observations. First, laboratory measurements and analyses of light scattering show that the real refractive index $\mathrm{Re}(m_{\mathrm{hyd}})$ (relative to seawater) of marine particulates is often bimodal, falling either between 1.02 and 1.09 or between 1.15 and 1.25.[19,67] The former mode is typical for living plankton[30] and organic cell debris with high (>60%) water content.[68] The latter mode is indicative of minerals from aeolian input[69] and inorganic cell debris with low (<25%) water content.[68] While intermediate values of refractive indices have been reported,[22,70] it is convenient to confine $\mathrm{Re}(m_{\mathrm{hyd}})$ to these modes, and to use the corresponding boundaries to define two particulate components of oceanic matter: phytoplankton [$1.02 \leq \mathrm{Re}(m_{\mathrm{hyd}}) \leq 1.09$] and high-refractive detritus [$1.15 \leq \mathrm{Re}(m_{\mathrm{hyd}}) \leq 1.25$]. We will denote the refractive index values of these components by m_{plk} and m_{det}, respectively, and assume them to be independent of λ for visible light. The corresponding scattering matrices will be referred to as $\mathbf{F}_{\mathrm{plk}}$ and $\mathbf{F}_{\mathrm{det}}$, respectively. Usually, one must specify also the imaginary part $\mathrm{Im}(m_{\mathrm{hyd}})$ of the refractive index in order to obtain the single scattering albedo from Mie computations. However, the bio-optical equations already provide us with the quantities necessary to compute this parameter, including its dependence on [Chl] and λ. Furthermore, $\mathrm{Im}(m)$ is usually less than 10^{-2} for marine particulates,[31] at which its impact on q_p

becomes negligible.[21] In what follows, we therefore set $\mathrm{Im}(m_{\mathrm{hyd}})$ to zero and use m_{hyd} to denote $\mathrm{Re}(m_{\mathrm{hyd}})$.

Second, measurements of the differential size distribution $n_{\mathrm{hyd}}(r)$ of ocean particulates are often found to follow a power-law (or Junge-type) distribution (Stramski and Kiefer[15] and references therein), i.e.,

$$n_{\mathrm{hyd}}(r) = Cr^{-\gamma_{\mathrm{hyd}}}, \tag{20}$$

where $\mathrm{d}n_{\mathrm{hyd}}(r)$ is the number of particles per unit volume with radius between r and $r + \mathrm{d}r$, and the constant C is chosen such that

$$\int_0^\infty n_{\mathrm{hyd}}(r)\mathrm{d}r = 1. \tag{21}$$

The value of the exponent γ_{hyd} in Eq. (20) varies in the majority of cases between 3.0 and 5.0 (Fig. 10 in Jonasz[71]). Accordingly, we assume $3.0 \le \gamma_{\mathrm{hyd}} \le 5.0$ for each m_{plk} and m_{det}, and denote the corresponding values of γ_{hyd} by γ_{plk} and γ_{det}, respectively. Note that γ_{plk} and γ_{det} are allowed to differ from one another, i.e., the total differential particle size distribution becomes also a two-component model. Such models have been found to fit measured distributions better than single-component models.[72,73] The radius r of marine particulates can range from tens of nanometers for viruses to hundreds of micrometers for diatoms. There is unfortunately little information available on the size population of submicron particles, while incorporating large diatomlike particles in the computation of scattering matrices can be very time consuming. However, results obtained by Risović[73] and by Ulloa *et al.*[21] show that q_p becomes invariant for particles with $r_{\min} \le 0.025$ μm, and that particles with $r_{\max} \ge 50$ μm contribute less than 1% to q_p. We therefore set $r_{\min}$ and $r_{\max}$ to 0.01 and 100 μm, respectively, for Eqs. (20) and (21).

Third, measurements of $\mathbf{F}_p$ performed for various open ocean samples[61,74] and phytoplankton cultures[17,62] show that its linear polarization percentage $-F_{21}/F_{11}$ remains relatively stable, exhibiting a bellshaped curve as a function of the scattering angle similar to that of Rayleigh–Gans scattering. The maximum value of this curve and its position were seen to vary from 0.6 to 0.8 and from 87° to 97°, respectively. The corresponding numbers for pure seawater are 0.84 and 90°, i.e., the $-F_{21}/F_{11}$ values of $\mathbf{F}_w$ can be taken as an *upper bound* for those of $\mathbf{F}_p$. These observations provide valuable constraints for $(m_{\mathrm{plk}}, \gamma_{\mathrm{plk}})$ and $(m_{\mathrm{det}}, \gamma_{\mathrm{det}})$. For example, it is common[15] in underwater light modeling to take $m_{\mathrm{plk}} \le 1.06$ from laboratory measurements results and to assume that $\gamma_{\mathrm{plk}} = 4$. The corresponding q_p are less than 0.009, i.e., smaller than observed for strongly oligotrophic ($[\mathrm{Chl}] \approx 0.03$ mg m^{-3}) ocean waters (e.g., Ulloa *et al.*[21]). It has been suggested[15] that this deficiency in q_p is indicative of the presence in the open ocean of small ($r_{\max} \le 1.0$ μm), low-refractive ($m_{\mathrm{det}} \le 1.05$) detritus particles that have a high q_p. However, the scattering matrix of both these plankton and detritus particles exhibit $-F_{21}/F_{11}$ values that are in excess of 0.92, which is too high even if one were to correct this number for nonspherical effects (see Voss and Fry[61]). Note that mixtures of such particles will then also lead to polarized water-leaving radiances that are (much) higher than observed in remote sensing data. Instead, we vary both sets of parameters $(m_{\mathrm{plk}}, \gamma_{\mathrm{plk}})$ and $(m_{\mathrm{det}}, \gamma_{\mathrm{det}})$ until F_{plk} and F_{det} show $-F_{21}/F_{11}$ values that are similar to those of $\mathbf{F}_w$. For simplicity, we will refer to the $-F_{21}/F_{11}$ values of $\mathbf{F}_{\mathrm{hyd}}$ (that is, of $\mathbf{F}_{\mathrm{plk}}$ or of $\mathbf{F}_{\mathrm{det}}$) as p_{hyd}, to those of $\mathbf{F}_w$ as p_w, and for future reference to those of $\mathbf{F}_{\mathrm{blk}}$ as p_{blk}. Hence the requirement put forward here is that p_{hyd} is approximately equal to p_w, which is the maximum observed in case 1 waters. We will discuss in Subsection 3.A another bimodal hydrosol model whose $-F_{21}/F_{11}$ values constitute a possible lower bound for those observed in the open ocean. The total particulate scattering matrix $\mathbf{F}_p$ can be derived from $\mathbf{F}_{\mathrm{plk}}$ and $\mathbf{F}_{\mathrm{det}}$ using

$$\mathbf{F}_p(\Theta, \lambda) = \frac{(1 - f_{\mathrm{det}})\sigma_{\mathrm{plk}}(\lambda)\mathbf{F}_{\mathrm{plk}}(\Theta, \lambda) + f_{\mathrm{det}}\sigma_{\mathrm{det}}(\lambda)\mathbf{F}_{\mathrm{det}}(\Theta, \lambda)}{(1 - f_{\mathrm{det}})\sigma_{\mathrm{plk}}(\lambda) + f_{\mathrm{det}}\sigma_{\mathrm{det}}(\lambda)}, \tag{22}$$

where f_{det} is the fraction of the total number of particles that is detritus, and σ_{plk} and σ_{det} are the scattering cross sections ($\mu\mathrm{m}^2$) obtained from Mie computations for $(m_{\mathrm{plk}}, \gamma_{\mathrm{plk}})$ and $(m_{\mathrm{det}}, \gamma_{\mathrm{det}})$, respectively. Note that

$$q_p(\lambda) = \frac{(1 - f_{\mathrm{det}})\sigma_{\mathrm{plk}}(\lambda)q_{\mathrm{plk}}(\lambda) + f_{\mathrm{det}}\sigma_{\mathrm{det}}(\lambda)q_{\mathrm{det}}(\lambda)}{(1 - f_{\mathrm{det}})\sigma_{\mathrm{plk}}(\lambda) + f_{\mathrm{det}}\sigma_{\mathrm{det}}(\lambda)}, \tag{23}$$

where q_{plk} and q_{det} are the backscattering efficiencies defined similarly to q_p in Eq. (10) except for using the scattering functions $\mathbf{F}_{\mathrm{plk}}$ and $\mathbf{F}_{\mathrm{det}}$, respectively. That is, f_{det} can be determined from q_p which is given by Eq. (12) as a function of [Chl] and λ. We will compute $\mathbf{F}_{\mathrm{plk}}$ and $\mathbf{F}_{\mathrm{det}}$ for $\lambda = 550$ nm and assume them and the corresponding scattering cross sections to be invariant for $400 \le \lambda \le 600$ nm. We shall see later that such assumptions still lead to good results for A_{blk} if, in Eq. (12) λ is chosen midway between 400 and 550 nm.

D. Multiple Scattering in the Atmosphere–Ocean System

Let $\tilde{\mathbf{I}}_0$ denote the specific intensity vector of a unidirectional beam of sunlight illuminating the Earth's atmosphere in the direction of $\mathbf{k}_0$ defined by the solar zenith angle θ_0 and azimuth angle φ_0. Also, let $\mu_0 = \cos\theta_0$. To describe the specific intensity vector $\tilde{\mathbf{I}}$ of light reflected by the atmosphere–ocean system, we proceed as follows. First, let $\mathbf{k}$ given by (μ, φ) denote the direction of light propagation for $\tilde{\mathbf{I}}$. We

choose the meridional plane for $\mathbf{k}$ (i.e., the plane containing the z axis and $\mathbf{k}$) as the reference plane for the parameters of $\tilde{\mathbf{I}}$ and do the same for $\mathbf{k}_0$ and $\tilde{\mathbf{I}}_0$. Then, following Hansen and Travis,[1] we define the (4×4) reflection matrix $\mathbf{R}(\mu, \varphi; \mu_0, \varphi_0)$ from

$$\pi\tilde{\mathbf{I}}(\mu, \varphi) = \mu_0\mathbf{R}(\mu, \varphi; \mu_0, \varphi_0)\tilde{\mathbf{I}}_0(\mu_0, \varphi_0). \quad (24)$$

Note that for the type of scattering matrices given by Eq. (5), only differences in the azimuthal angle are relevant because of the rotational symmetry with respect to the z axis. This implies that $\mathbf{R}(\mu, \varphi; \mu_0, \varphi_0) = \mathbf{R}(\mu, \mu_0; \varphi - \varphi_0)$. The AOS reflection matrix thus defined incorporates all scattering processes that occur in the atmosphere–ocean system, and can be obtained relatively easily from the corresponding reflection and transmission matrices for the atmosphere, ocean surface, and ocean body components using the adding method.[75] We adopt this method, and complement it according to the work by de Haan *et al.*[76] and Chowdhary.[77] The former work presents a detailed study on the adding method for planetary atmospheres and applies new features such as a special Fourier expansion for the adding equations and a so-called product method for the repeated reflections between two layers. The latter work builds on this study and discusses modeling problems that arise when including the ocean surface and ocean body and their remedies.

The atmosphere–ocean system specification for our radiative transfer computations allows the ocean body to be subdivided into a number of plane-parallel, optically homogeneous layers, and to have a Lambertian bottom with albedo A_{bot}. The user-provided scattering properties for each of these layers include: the bulk optical thickness $\Delta\tau_{\text{blk}}$; the scattering coefficients b_w and b_p of water and particulate matter, respectively; the depolarization factor δ_w of ocean water; and the bulk absorption coefficient a_{blk}. In addition, expansion coefficients of the particulate scattering matrix $\mathbf{F}_p$ in terms of generalized spherical functions[78] are given. For the current study, we assume the ocean body to consist of a single layer with an optical thickness $\Delta\tau$ of 10 and no bottom (i.e., $A_{\text{bot}} = 0$). The reason for this is that while it is usual for the vertical chlorophyll profiles of oligotrophic oceans to develop a maximum below the nutrient-depleted mixed layer,[79] most of the water-leaving radiance originates from scattering in the top ($z \geq -60$ m) layer.[80] The latter layer was found to have an optical thickness of less than 8 for $\omega_{\text{blk}} \leq 0.9$, and can be approximated by a homogeneous layer if the chlorophyll maximum resides lower than -45 m or if $[\text{Chl}] \geq 0.4$ mg/m^3 near the ocean surface.[81]

The specification and computations for the atmosphere are similar to those for the ocean body with the following exceptions. The user-provided scattering properties for each atmospheric layer are the molecular scattering and absorption optical thickness $\Delta\tau_{\text{mol,sca}}$ and $\Delta\tau_{\text{mol,abs}}$ respectively; the molecular depolarization factor δ_{mol}; the aerosol extinction optical thickness $\Delta\tau_{\text{aer,ext}}$; the aerosol single scattering albedo ω_{aer}; and the expansion coefficients of the aerosol scattering matrix in terms of generalized spherical functions. Our radiative transfer program allows for the option to retrieve the upwelling internal radiation field in the atmosphere (to analyze aircraft observations as in Chowdhary *et al.*[6,10,82]) rather than at the top of the atmosphere. We therefore also specify for each atmospheric layer whether it is situated above or below the observer. Here we will study only the radiation field emerging from the top of a molecular (i.e., homogeneous) atmosphere. While such pristine atmospheres occur rarely, we want to examine first the variation in magnitude and bidirectional behavior of the water-leaving radiances as a function of wavelength and chlorophyll a concentration before including the highly variable effects of aerosol scattering.

The reflection and transmission matrices of the ocean surface are derived from the Gaussian-distributed slope distribution given by Cox and Munk.[83] The user-provided surface properties are the windspeed W (m s^{-1}) at 10 m above the surface, and the (complex) refractive index m_{srf} relative to air. Optional features include the correction for shadowing effects,[84] scattering by ocean foam with user-provided foam albedo A_{fm},[85,86] and the wind-direction ψ for computations of the direct (i.e., not scattered by the atmosphere) sunglint contribution.[83] Note that the ocean surface matrices thus obtained do not account for multiple scattering by adjacent waves.[87] Also, we use N_s and N_w Gaussian quadrature points for skylight and underwater light scattering, respectively, the directions of which are not related by Snell's law. To correct for the resulting energy deficiency η, the ocean surface transmission matrix is normalized along the two directions closest to the refraction peak for a smooth surface, and a modified version of Hansen's[88] iterative normalization method is used to update the ocean surface reflection matrix. The partitioning of η amongst these matrices is based on the flux transmitted and reflected by a smooth surface. This approach leads to good results for $N_s, N_w \geq 20$ if the windspeed is fixed at 7 m s^{-1} for ocean surface transmission only, and allows the underwater light field computations to be decoupled from those for the skylight.[77] Note that water-leaving radiances depend very little on the ocean surface roughness[29,89,90] as opposed to the skylight reflected off this surface, and that for most polarimetric applications $N_s, N_w > 20$ in order for the computations to be sufficiently accurate. For this study, we take shadowing effects into account, include the presence of foam, ignore wind directionality, and adopt $W = 7$ m s^{-1} for the ocean surface wind.

In addition to upwelling radiation in the atmosphere, the skylight field just above the surface is also provided. The matrix describing this field is rendered either as a by-product when adding the entire atmosphere to the ocean system, or updated using the

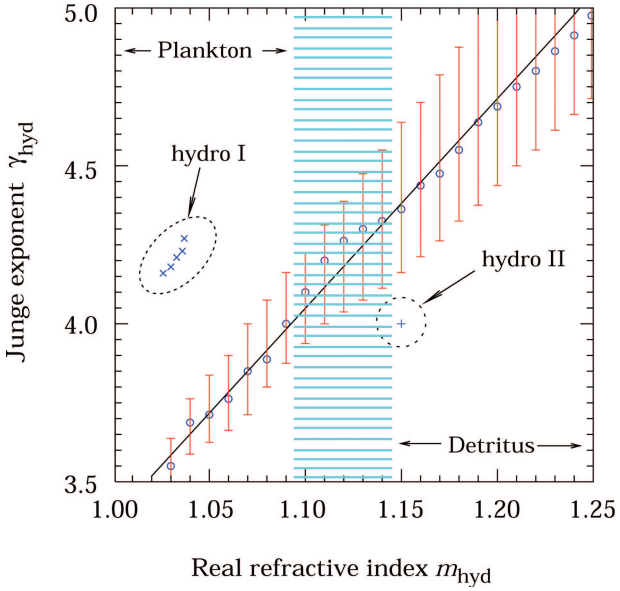

Fig. 2. (Color online) On the relation between the Junge exponent γ_{hyd} and refractive index m_{hyd} of hydrosol particles. Circles, results obtained from minimizing Eq. (25). Error bars, range for which $d \leq d_{min} + 1\%$ in Eq. (25). Solid line, line given by Eq. (26) to fit circles. Hydro I and II, results obtained from other considerations (see text).

method described by Stamnes *et al.*[91] when adding an additional layer to the atmosphere to retrieve its internal upwelling radiation. The radiative transfer program accepts further the option to decompose all radiation fields into scattering contributions originating from the atmosphere, ocean surface, and ocean body. We invoke the latter option when studying the contribution of water-leaving radiances to top-of-the-atmosphere (TOA) observations in Subsection 3.C. Extensive tests have been performed to validate the computational output. Internal tests include monitoring the conservation of energy, verifying that $\mathbf{R}(\mu, \mu_0; \varphi - \varphi_0)$ and other atmosphere–ocean system matrices obey the symmetry rules given by Hovenier,[92] and comparing results obtained for different specifications of identical atmosphere–ocean systems. The external tests include comparing results with those computed according to Mishchenko and Travis[3] and Jin *et al.*[93] for atmosphere–ocean systems, with those tabulated by Hovenier and de Haan,[94] and de Haan *et al.*[76] for atmospheres, and with field measurements obtained 25 km off the coast of Virginia during the Chesapeake Lighthouse and Aircraft Measurements for Satellites (CLAMS) experiment.[82]

3. Results and discussion

A. Hydrosol Models for Case 1 Waters

Figure 2 shows the results (open circles) for the retrieval of plankton ($m_{hyd} \leq 1.09$) and detritus ($m_{hyd} \geq 1.15$) particle properties. The retrieval is based on a least-squares fit method in which γ_{hyd} is varied for given m_{hyd} until

$$d = \sqrt{\frac{1}{N}\sum_{i=1}^{N} h[p_{hyd}(\Theta_i) - p_w(\Theta_i)]^2} \qquad (25)$$

attains its minimum d_{min}. In Eq. (25), $0° \leq \Theta_i \leq 180°$ and $|\Theta_i - \Theta_{i-1}| = 1°$ so that $N = 181$. Also, $h = 4$ for Θ_i if for this angle $p_{hyd} \geq 85\%$ and 1 if otherwise to avoid solutions for which $p_{hyd} \gg p_w$. The error bars correspond to solutions with $d \leq d_{min} + 1\%$ and provide a measure for the sensitivity of p_{hyd} to γ_{hyd} for given m_{hyd}. Conversely, they present reasonable ranges for γ_{hyd} if $p_{hyd} \approx p_w$, or upper bounds for γ_{hyd} if $p_{hyd} < p_w$, when using monomodal hydrosol models for underwater light computations. The solid line in Fig. 2 is given by

$$\gamma_{hyd} = 6.63 m_{hyd} - 3.25 \quad (\pm 0.05) \qquad (26)$$

and provides a simple but useful parameterization of our solutions for $1.03 \leq m_{hyd} \leq 1.25$. The corresponding results for p_{hyd} are shown in Figs. 3(a) and 3(b), where we also included the values for p_w. Because of the strong similarities of linear polarization for $m_{hyd} \geq 1.15$, only two cases are shown for this group in Fig. 3(b). The dotted line in these figures corresponds to $-F_{21}/F_{11} = 85\%$, which is the upper limit for p_{hyd} used in Eq. (25).

To illustrate our motive for using Eq. (25) to constrain γ_{hyd}, we also computed γ_{hyd} and m_{hyd} using only the extinction coefficient $c_p \equiv a_p + b_p$ (m^{-1}) and the backscattering efficiency q_p, respectively, according to the method described by Twardowski *et al.*[22] Note that this method assumes the hydrosol particles to be monomodal. We employed for this purpose the absorption coefficient given by Morel and Gentili[34]:

$$a_p(\lambda) = 0.06\, A(\lambda)[\mathrm{Chl}]^{0.65}, \qquad (27)$$

where $A(\lambda)$ is the specific absorption coefficient normalized to the one for $\lambda = 440$ nm and tabulated by Prieur and Sathyendranath.[51] The results (referred to "hydro I" particles) for $\lambda = 550$ nm are shown in Fig. 2 for [Chl] = 0.03, 0.1, 0.3, 1.0, and 3.0 mg m^{-3}, and in Fig. 3(b) for [Chl] = 0.3 mg m^{-3}. Observe now how the values for γ_{hyd} are much higher than those obtained by minimizing Eq. (25), leading to $p_{hyd} \gg p_w$. We remark on the other hand, that analyses performed by Twardowski *et al.*[20] for data obtained for the upper ($z \leq 50$ m) layers of the Gulf of California result into (m_{hyd}, γ_{hyd}) pairs that vary from (1.05, 4.0) to (1.08, 3.7), which is only slightly larger than the range denoted by the error bars in Fig. 2. The conclusion to be drawn here is that the bio-optical equations for $a_p(\lambda)$ and $b_p(\lambda)$ contain too large uncertainties in the description of their spectral behavior to provide useful information on γ_{hyd} (for example, the λ^{-1} dependency for b_p is explicitly assumed in Morel[8]), even though substituting $b_p(\lambda)$ in Eqs. (8) and (9) leads to realistic values of $A_{blk}(\lambda)$. This problem is circumvented in the current study by using p_w, rather than extinction spectra, to retrieve γ_{hyd}. It should

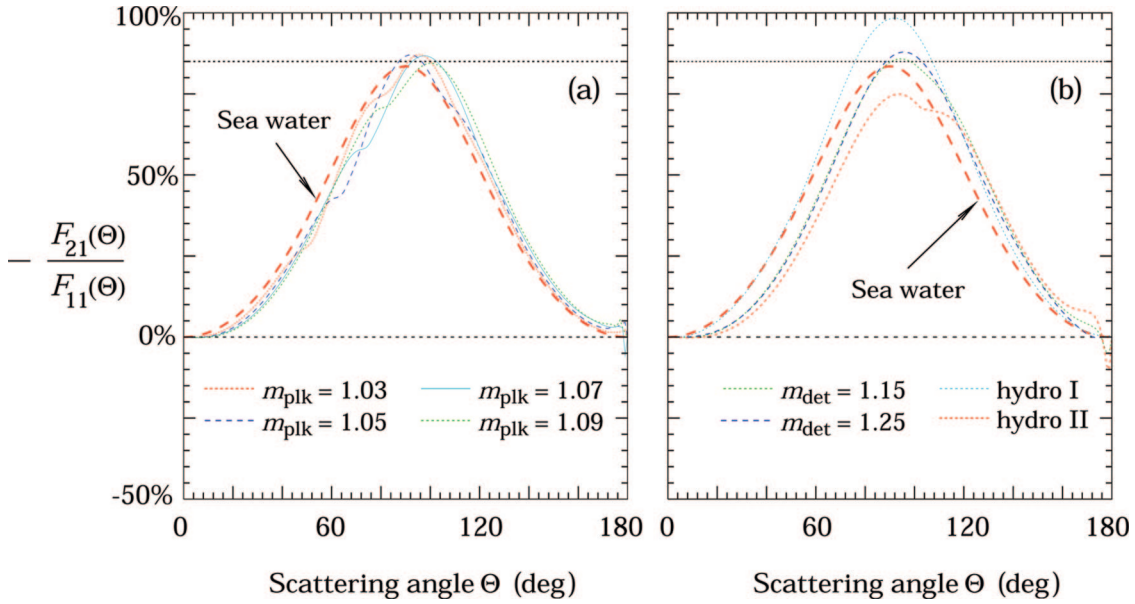

Fig. 3. (a) Degree of linear polarization for single scattering of unpolarized light. The dashed red line corresponds to scattering by pure seawater (p_w). The lines for m_{plk} are for scattering by hydrosol particles with $m_{hyd} = m_{plk}$ and γ_{hyd} given by Eq. (26). (b) Same as (a) except for $m_{hyd} = m_{det}$. Also shown are cases for the hydro I and II particles defined in Fig. 2.

once again be stressed that Eq. (26) provides only real solutions for bimodal hydrosols whose p_{hyd} exhibit about the same values as those of p_w. That is, it *is* possible to encounter hydro I-type particles in open ocean waters and at the same time observe that $-F_{21}/F_{11} \le p_w$ for the underwater light; they are then accompanied by particles with $p_{hyd} \ll p_w$ such as those with properties denoted by "hydro II" in Figs. 2 and 3(b). In addition, one may encounter hydrosol particles that *all* exhibit $p_{hyd} < p_w$ (e.g., Adams *et al.*[95]). However, there exists little information to parameterize such variation of p_{hyd} other than $-F_{21}/F_{11} \le p_w$ for bulk case 1 waters. Hence Eq. (26) provides a simple tool when combined with the bio-optical model of case 1 waters to simulate the *maximum* of linearly polarized water-leaving radiances as might be observed from an aircraft or spacecraft for given A_{blk}. As more information becomes available on the variation of underwater light polarization, one may substitute p_w in Eq. (25) with such data to obtain corresponding variations of Eq. (26).

Figure 4(a) provides a representative set of scattering functions for the solutions given by Eq. (26). The corresponding backscattering efficiencies are given in Fig. 5 for $m_{hyd} \le 1.12$ with errors bars retrieved from those in Fig. 2. We remark that these backscattering efficiencies constitute an upper bound for case 1 waters; lower values for given m_{hyd} such as those found by Twardowski *et al.*[22] imply that $-F_{21}/F_{11} < p_w$ for the underwater light. The dashed lines in Fig. 5 are for the minimum ($q_{p,min}$) and maximum ($q_{p,max}$) value of q_p according to Eqs. (12) and (13) as [Chl] varies from 3.0 to 0.03 mg m^{-3} while $410 \le \lambda \le 600$ nm [see also Fig. 6(a)]. Note that q_{plk} must be smaller than or equal to $q_{p,min}$, and q_{det} larger than or equal to $q_{p,max}$, for Eq. (23) to reproduce the full range of $q_{p,min} \le q_p \le q_{p,max}$. All the detritus scattering functions shown in Fig. 4(a) satisfy the latter criterion for q_{det}. However, Fig. 5 shows that the plankton models derived from Eq. (26) satisfy $q_{plk} \le q_{p,min}$ only if $m_{hyd} \le 1.06$. We choose $m_{plk} = 1.04$ and $m_{det} = 1.15$. The Junge exponents for these two choices are, according to Eq. (26), $\gamma_{plk} = 3.7$ and $\gamma_{det} = 4.4$ (rounded off to the nearest decimal), respectively. The corresponding cross sections σ_{plk} and σ_{det}, and backscattering efficiencies q_{plk} and q_{det}, are given in Table 1. Note though that any $1.03 \le m_{hyd} \le 1.06$ can be chosen for m_{plk}, and similarly that any $1.15 \le m_{hyd} \le 1.25$ suffices for m_{det}, as input for Eq. (26) to obtain viable hydrosol components for case 1 waters. Consequently, there are many bimodal hydrosol solutions, each of which can be identified by a unique pair of refractive indices (m_{det}, m_{plk}). We will refer to the collective of hydrosol components and their mixtures of each such solution as a detritus and plankton particles (D–P) mixture. For the number fractions f_{det} of each D–P mixture we require q_p in Eq. (23) to be 0.0138, 0.0109, 0.0087, 0.0071, and 0.0058 for [Chl] = 0.03, 0.1, 0.3, 1.0, and 3.0 mg m^{-3}, respectively. These values of q_p (see also Table 2) are consistent with the ones given by Eq. (12) for corresponding [Chl] and $410 \le \lambda \le 550$ nm [Fig. 6(a)], and lead to excellent agreements between Eqs. (7) and (8), as will be shown in Subsection 3.B. The values for f_{det} retrieved in this manner for the D–P mixture specified in Table 1, which we designate as our reference hydrosol model, are given in Table 2. They can be nicely reproduced as a function of [Chl] from the following fit [Fig. 6(b)]:

$$f_{det}(\mathrm{Chl}) = 0.91[\mathrm{Chl}]^{-0.08} - 0.49 \quad (\pm 0.015), \quad (28)$$

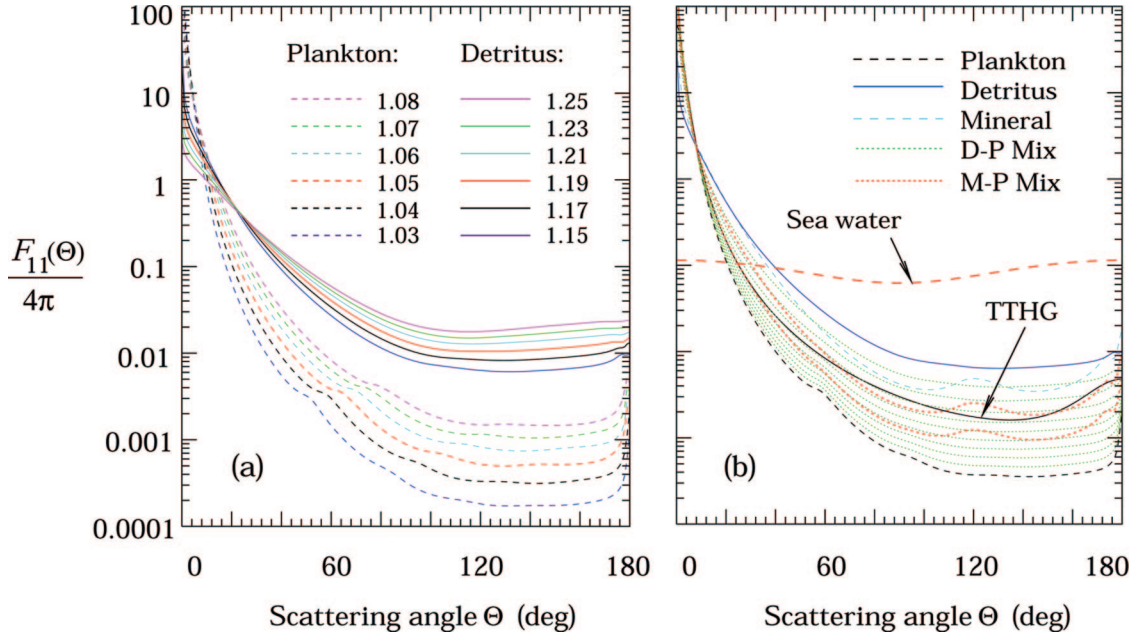

Fig. 4. (a) Scattering functions (normalized by 4π) for hydrosol particles with m_{hyd} and γ_{hyd} provided by the legend and Eq. (26), respectively. (b) Same as (a) except for the plankton, detritus, and mineral particles specified in Table 1. Also shown are cases for the mixture of detritus and plankton particles (D–P Mix), for the mixture of mineral and detritus particles (M–P Mix), for the TTHG used by Walker (Ref. 89) to fit Petzold's (Ref. 13) measurements, and for scattering by pure seawater. The cases for the D–P mixture correspond to $f_{det} = 0.1, 0.2, \ldots, 0.8, 0.9$.

which states that the relative abundance of small, highly reflective detritus particles decreases as [Chl] increases. Such behavior is consistent with observed relationships between the particle size and phytoplankton abundance as mentioned in Morel *et al.*[42]

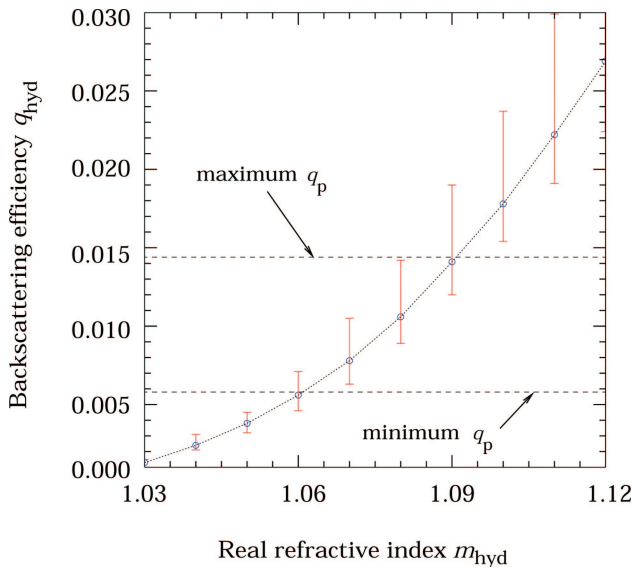

Fig. 5. (Color online) On the relation between the backscattering efficiency q_{hyd} and hydrosol refractive index m_{hyd}. Circles, results obtained from the Mie theory with γ_{hyd} given by Eq. (26). Error bars, range in q_{hyd} corresponding to the range in γ_{hyd} shown in Fig. 2 by the error bars. Minimum q_p, smallest backscattering efficiency for [Chl] = 3.0 mg/m^3 and $410 \leq \lambda \leq 600$ nm according to Eq. (12). Maximum q_p, largest backscattering efficiency for [Chl] = 0.03 mg/m^3 and $410 \leq \lambda \leq 600$ nm according to Eq. (12).

Substitution of Eq. (28) into Eq. (22) provides the change of F_p with [Chl] for this D–P mixture. To illustrate this change, we provide the variation of F_p with f_{det} in Fig. 4(b) (green-dotted lines), where f_{det} corresponds to 0.1, 0.2, . . . , 0.8, 0.9. The perspective numbers for [Chl] are found from inverting Eq. (28).

For comparison, we included in Fig. 4(b) the fit obtained by Walker[89] using two-term Henyey-Greenstein (TTHG) functions[96] for the particulate scattering functions measured by Petzold[13] in clear ocean waters (i.e., his AUTEC and HOACE data sets). The asymmetry parameters g_1 and g_2 for this fit are 0.95 and −0.7; the corresponding weights w_1 and w_2 are 0.9975 and 0.0025, respectively. Note that this fit exhibits a broad enhancement in scattering toward the backward ($\Theta = 180°$) direction. This feature is much narrower for our D–P mixture, and although there are measurements of such narrow, so-called glory features (e.g., Lee and Lewis[97]), other data (e.g., Kullenberg[98]) support the broad glory exhibited by the TTHG fit. To evaluate the effect on water-leaving radiances of these variations in glory, we consider also hydrosol blends of *mineral* and plankton particles (hereafter referred to as M–P mixtures). We adopt for the mineral particles a lognormal size distribution[1] with effective radius r_{eff} and effective variance v_{eff} given by 1.0 μm and 5.0, respectively, and a refractive index m_{mnr} given by 1.20. The resulting scattering function F_{mnr} is shown in Fig. 4(b) (blue-dashed line). Note that while our choices for r_{eff} and v_{eff} are much larger than the ones for the mineral particles in seawater modeled by Woźniak and Stramski,[69] they cause F_{mnr} to exhibit a broad glory

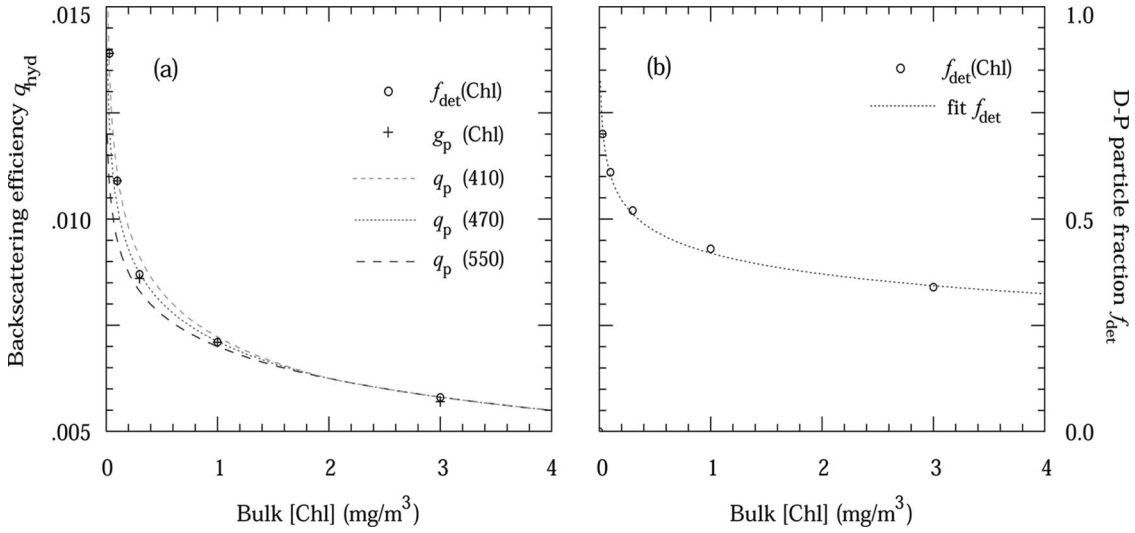

Fig. 6. (a) On the relation between the backscattering efficiency q_{hyd} and the chlorophyll a concentration [Chl]. q_p: backscattering efficiency provided by Eq. (12) as a function of λ and [Chl]. Circles, backscattering efficiency for the D–P mixture specified in Table 1 and f_{det} given by Table 2. Pluses, backscattering efficiency for a one-term Henyey–Greenstein function with varying asymmetry parameter g_p (see Fig. 9). (b) The change in particle fraction f_{det} with chlorophyll a concentration [Chl]. Circles, f_{det} values given in Table 2. Dotted line, line given by Eq. (28) to fit circles.

similar to that shown by the TTHG fit. The scattering cross section σ_{mnr} and backscattering efficiency q_{mnr} (defined similarly to q_p except for using F_{mnr}) for this M–P mixture are given in Table 1. Also shown in Fig. 4(b) are two scattering functions F_p for this mixture (red-dotted lines) corresponding to [Chl] = 0.03 and 1.0 mg m^{-3}. The fractions f_{mnr} of particles that are mineral for these and other values of [Chl] are listed in Table 2.

The variation of $-F_{21}/F_{11}$ with [Chl] is shown in Fig. 7 for the D–P and M–P mixtures of Table 1. The results in Figs. 7(a) and 7(b) are for the $\mathbf{F}_p$ and $\mathbf{F}_{blk}$ scattering matrices, i.e., for excluding and including seawater, respectively. The $-F_{21}/F_{11}$ values for $\mathbf{F}_{plk}$, $\mathbf{F}_{det}$ and $\mathbf{F}_{mnr}$ are also shown in Fig. 7(a) for comparison, and similarly for $\mathbf{F}_w$ in Fig. 7(b). The D–P curves in Fig. 7(a) correspond to [Chl] = 0.3 and 30 mg m^{-3}. They lie, as intended, close to one another and to the $-F_{21}/F_{11}$ values for $\mathbf{F}_{plk}$ and $\mathbf{F}_{det}$. The change of $-F_{21}/F_{11}$ with [Chl] becomes even less noticeable for this D–P mixture when including seawater; hence only one such example (corresponding to [Chl] = 0.3 mg m^{-3}) is shown in Fig. 7(b) (D–P Bulk). The small sensitivity to [Chl] is the result of the requirement $p_{hyd} \approx p_w$ posed in Eq. (25), which causes *any* mixture of hydrosols and seawater to exhibit $-F_{21}/F_{11}$ values similar to those of $\mathbf{F}_w$. The $-F_{21}/F_{11}$ values for $\mathbf{F}_{mnr}$ on the other hand are much smaller from those obtained for $\mathbf{F}_{plk}$. Consequently, one can clearly see $-F_{21}/F_{11}$ grow steadily for the M–P mixture in Fig. 7(a) as [Chl] increases from 0.03 to 3.0 mg m^{-3}. The variation with [Chl] becomes, however, complicated for this M–P mixture when adding seawater. This is because the change of b_p with [Chl] in Eq. (11) is opposite in sign to that of F_p with [Chl] in Fig. 4(b), which causes F_{blk} in Eq. (18) to oscillate with increasing [Chl]. Rather than discussing in detail the resulting fluctuations in $-F_{21}/F_{11}$ values, we simply provide in Fig. 7(b) their lower limit (M–P Bulk corresponding to [Chl] = 1.0 mg m^{-3}) and upper limit (M–P Bulk corresponding to [Chl] = 0.03 mg m^{-3}) for the [Chl] values listed in Table 1. Finally, we remark that the M–P curves in Fig. 7(b) exhibit a smaller maximum than the ones measured in case 1 waters for sideward-scattering angles[61] except perhaps for near the coast,[95] and that they can contain a second local maximum closer to the backscattering direction. This implies that the *differences* in polarized water-

Table 1. Reference D–P and M–P Mixtures

	Plankton	Detritus	Mineral
Size distribution[a]	Junge	Junge	Lognormal
	$\gamma_{plk} = 3.7$	$\gamma_{det} = 4.4$	$r_{eff} = 1.0$
			$v_{eff} = 5.0$
Refractive index	$m_{plk} = 1.04$	$m_{det} = 1.15$	$m_{mnr} = 1.20$
Scattering properties[b]	$\sigma_{plk} = 8.874 \times 10^{-5}$	$\sigma_{det} = 1.388 \times 10^{-5}$	$\sigma_{mnr} = 2.186 \times 10^{-2}$
	$q_{plk} = 2.663 \times 10^{-3}$	$q_{det} = 4.444 \times 10^{-2}$	$q_{mnr} = 2.581 \times 10^{-2}$

[a] r_{eff} in μm.
[b] σ_{plk}, σ_{det}, and σ_{mnr} in μm^2.

Table 2. Mixing Ratios of the D–P and M–P Mixtures Referenced in Table 1

[Chl][a]	0.03	0.10	0.30	1.00	3.00
q_p	0.0138	0.0109	0.0087	0.0071	0.0058
f_{det}	0.70	0.61	0.52	0.43	0.34
f_{mnr}	0.00375	0.00224	0.00143	0.00096	0.00063

[a][Chl] in mg/m^3.

leaving radiances between the M–P and D–P ocean mixtures are consistent with (if not larger than) what one would expect for the actual range of p_{hyd} found in the open ocean.

B. Ocean Colors and Albedos

In Fig. 8 we compare results obtained from radiative transfer computations with predictions for the ocean color of case 1 waters. The hydrosol models used for the underwater light scattering computations are the D–P and M–P mixtures specified in Table 1 (see also Fig. 7), and the TTHG scattering function discussed in Subsection 3.A and shown in Fig. 4(b). As discussed in Subsection 2.D, we performed computations for a homogeneous ocean body with optical thickness $\Delta\tau = 10$, an ocean surface ruffled by a surface wind with $W = 7$ m/s, and a purely molecular atmosphere. The solar zenith angle θ_0 for Fig. 8 is 30°. The curves show the values of A_{blk} predicted by Eq. (8), where for α we used the parameterization given by Morel and Gentili.[34] The symbols denote results from radiative transfer computations at selected λ.

In Fig. 8(a), we consider only multiple scattering for fixed F_p, i.e., where the scattering function of the particulate matter is not allowed to vary with [Chl]. The circles in this panel correspond to computations for the Petzold-like[13] TTHG scattering function. Note that the results from these computations are reasonably close those predicted by the bio-optical model if [Chl] ≤ 0.1 mg/m^3 but that they also significantly overestimate A_{blk} for even moderately high [Chl]. Such shortcomings of Petzold's[13] data are caused by the relatively large value (>1.5%) of q_p for his scattering functions as discussed in Morel *et al.*[42] The additional picture that emerges from this figure, however, is that using such scattering functions can also cause the variation of A_{blk} with [Chl] to be either too large *or* too small by a factor of at least 2, depending on the wavelength. We also performed computations for $f_{\mathrm{det}} = 0.68$ of our D–P mixture, the results of which are shown by the plus symbols in this panel. We chose this value for f_{det} because it reproduces almost perfectly the results obtained for the TTHG scattering function. This confirms for a wide range of λ and [Chl] the conclusion by Mobley *et al.*,[40] namely, that A_{blk} depends little on the underwater light scattering function as long as $F_p(\Theta)$ remains approximately the same. From Fig. 4(b), we observe indeed that the TTHG function is similar to the scattering function of the D–P mixture member with $f_{\mathrm{det}} \approx 0.7$. Finally, we remark that it *is* possible to obtain good results for high [Chl] and fixed F_p by choosing a smaller f_{det}—note, for example, in Fig. 8(a) the agreement between computed and predicted values of A_{blk} for [Chl] = 3 mg/m^3 using $f_{\mathrm{det}} = 0.32$. However, the agreement then disappears for lower values of [Chl]

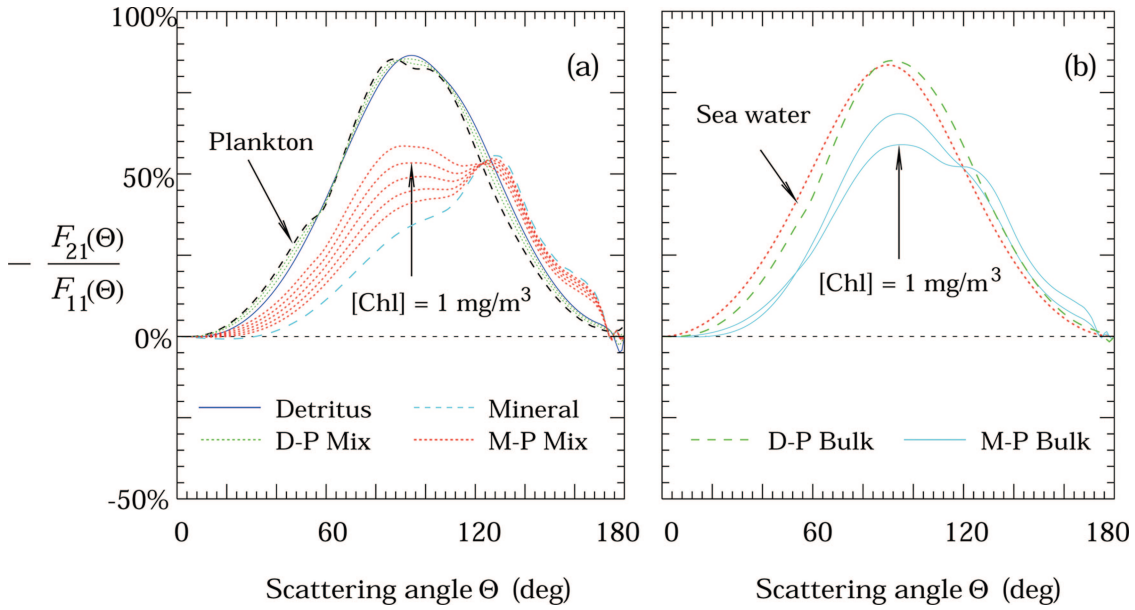

Fig. 7. (Color online) (a) Degree of linear polarization for single scattering of unpolarized light by the plankton, detritus, and mineral particles specified in Table 1. Also shown are cases for the mixture of detritus and plankton particles (D–P Mix), and for the mixture of mineral and detritus particles (M–P Mix). The cases for the D–P mixture correspond to [Chl] = 0.3 and 30.0 mg/m^3, while those for the M–P mixture to [Chl] = 0.03, 0.1, 0.3, 1.0, and 3.0 mg/m^3. (b) Same as (a) except for including scattering by seawater for the D–P mixture (D–P Bulk) and for the M–P mixture (M–P Bulk). The chlorophyll *a* concentration [Chl] is 0.3 mg/m^3 for the D–P bulk mixture, and 0.03 and 1.0 mg/m^3 for the M–P bulk mixture.

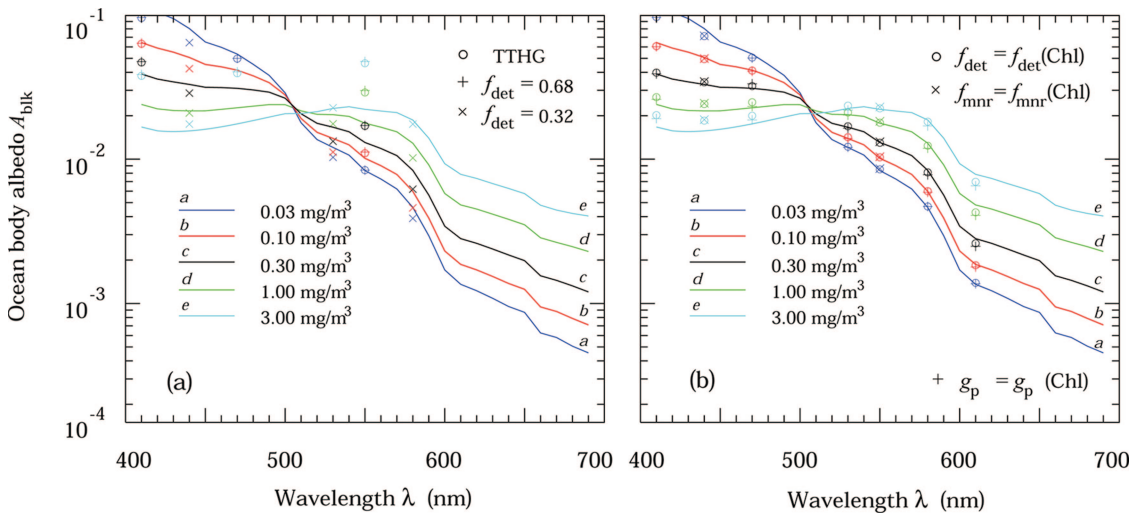

Fig. 8. (Color online) (a) The ocean body irradiance ratio A_{blk} just below the ocean surface as a function of λ and [Chl]. Curves, statistical predictions by the bio-optical model discussed in Subsection 2.B. Circles, radiative transfer (RT) results for the TTHG hydrosol scattering function of Fig. 4(b). Pluses, RT results for the mixture of plankton and detritus particles specified in Table 1 with f_{det} fixed at 0.68. Crosses, RT results for the mixture of plankton and detritus particles specified in Table 1 with f_{det} fixed at 0.32. (b) Same as (a) except for the following. Circles, RT results for the mixture of plankton and detritus particles specified in Table 1 with f_{det} varied according to Table 2. Crosses, RT results for the mixture of plankton and mineral particles specified in Table 1 with f_{mnr} varied according to Table 2. Pluses, RT results for a one-term Henyey–Greenstein function with varying asymmetry parameter g_p (see Fig. 9).

except perhaps for extreme oligotrophic oceans, where F_{blk} is least sensitive to F_p because of small b_p [cf. Eqs. (18) and (11), respectively].

The symbols in Fig. 8(b) denote results obtained when F_p is allowed to change such that its backscattering efficiency q_p varies with [Chl] as predicted by Eq. (12) [see also discussion of Fig. 6(a)]. The circles and crosses in this panel are for the D–P and M–P mixture, respectively, while the plus symbols correspond to a case in which F_p is represented by a one-term Henyey–Greenstein function. The asymmetry parameter g_p of the latter function was tuned to provide the same backscattering efficiency q_p as the D–P mixture for given [Chl] [Table 2 and Fig. 6(a)], and can be reproduced as a function of [Chl] by (Fig. 9, below):

$$g_p(\mathrm{Chl}) = 0.991 - 0.024[\mathrm{Chl}]^{-0.23} \quad (\pm 0.001). \tag{29}$$

We observe first from Fig. 8(b) that the irradiance ratios A_{blk} computed for any of these scattering functions are practically identical to one another for given [Chl] and λ. Hence the scattering functions apparently meet the condition that their overall shapes are similar to one another even though they differ somewhat in the backscattering direction. Figure 9 confirms that the asymmetry parameters of the D–P and M–P mixtures are very similar to g_p for all [Chl] considered. Second, the computed A_{blk} values agree quite well with their predicted values for 0.03 mg/m^3 ≤ [Chl] ≤ 3.0 mg/m^3 *and* for 400 nm ≤ λ ≤ 600 nm. The differences are reasonable if one considers that the computed values of A_{blk} ignore the wavelength dependency of q_p (which, according to Fig. 6(a), becomes significant for [Chl] < 1 mg/m^3), and that the predicted values of A_{blk} are sensitive to the parameterization of α and of μ_d. For example, the values of α provided at specific wavelengths by Morel *et al.*[42] lead to an excellent fit for all [Chl] if λ ≤ 500 nm but they also increase the prediction of A_{blk} for λ > 500 nm, and keeping μ_d fixed at 0.9 as in Morel[8] rather than deriving μ_d

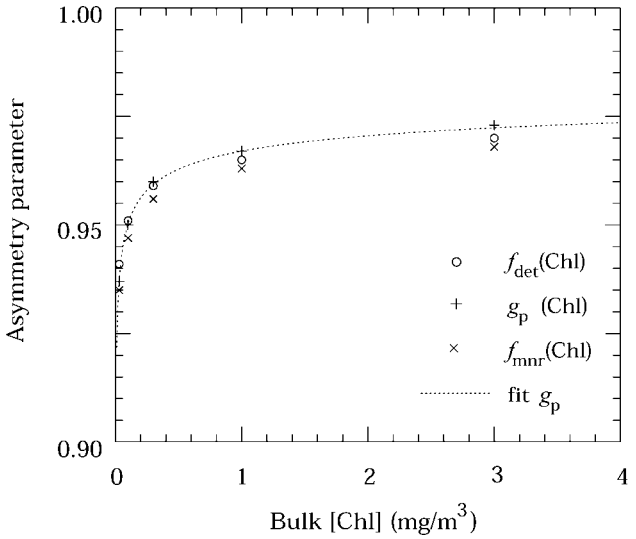

Fig. 9. On the relation between the asymmetry parameter of hydrosol particles and chlorophyll *a* concentration [Chl]. Circles results for the mixture of plankton and detritus particles specified in Table 1 with f_{det} varied according to Table 2. Pluses, values used for the one-term Henyey–Greenstein functions in Figs. 6(a) and 8(b). Crosses, results for the mixture of plankton and mineral particles specified in Table 1 with f_{mnr} varied according to Table 2. Dotted line, line given by Eq. (29) to fit crosses.

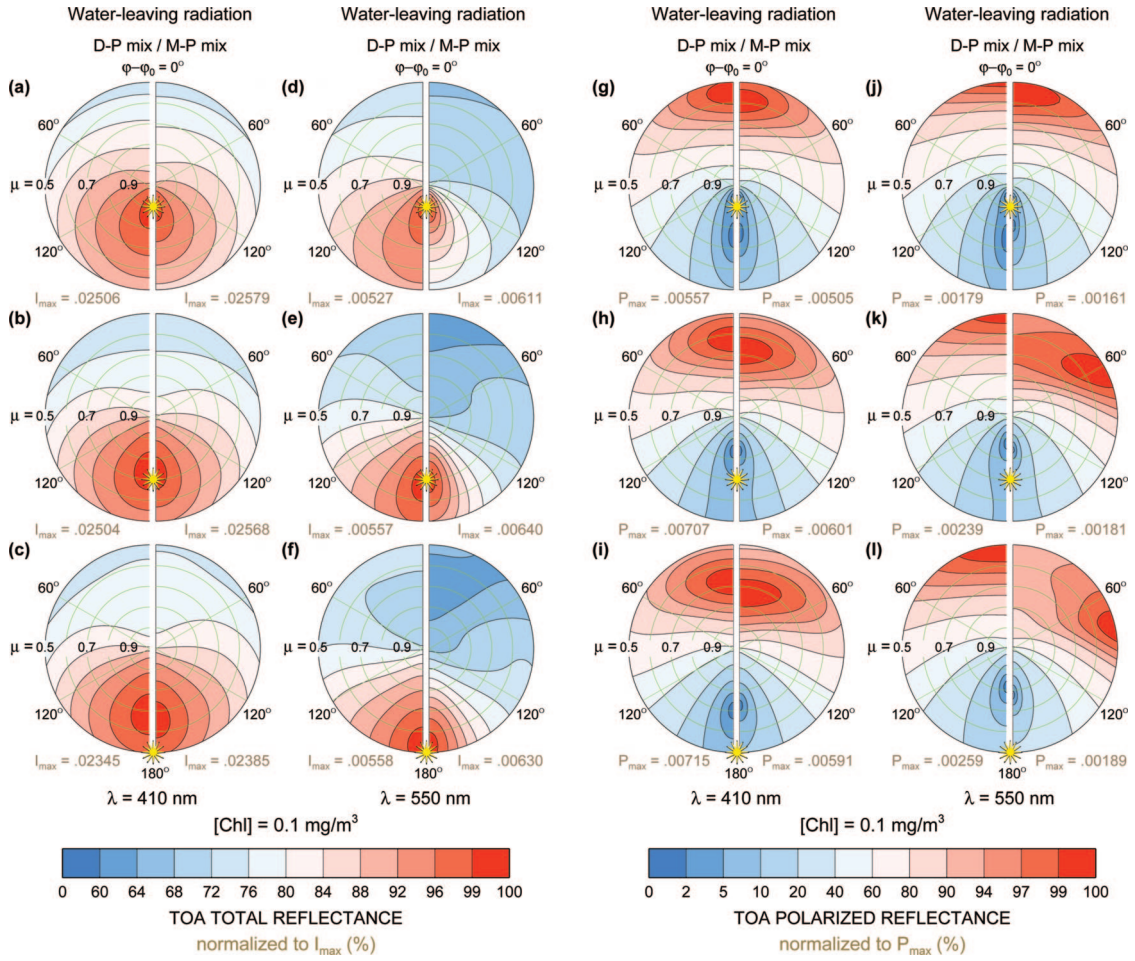

Fig. 10. Polar diagrams of the spaceborne total (first two columns) and polarized (last two columns) reflectance for water-leaving radiances normalized by I_{max} and P_{max}, respectively. Results are for an atmosphere–ocean system consisting of a molecular atmosphere that is bounded from below by an ocean system with $W = 7$ m/s and [Chl] = 0.1 mg/m^3. The solar zenith angle corresponds to $\mu_0 = 0.9$ (first row), 0.7 (second row), and 0.5 (third row), and is depicted by a yellow star in the antisolar point. The left- and right-hand-side hemispheres are for the D–P and M–P mixture, respectively, defined by Tables 1 and 2. The wavelength λ is 410 nm for diagrams (a)–(c) and (g)–(i), and 550 nm for diagrams (d)–(f) and (j)–(l).

from simulations with Petzold-like particulate scattering[99] decreases A_{blk} if $\lambda \leq 500$ nmor if [Chl] ≥ 1 mg/m^3. Note also that these differences are small compared to changes in A_{blk} caused by [cf. Eqs. (8) and (9)] the large natural variability in b_p (Loisel and Morel[79]) and in the particulate component of a_{blk} (Bricaud *et al.*[49]). We conclude that the scattering functions of the D–P and M–P mixtures specified in Table 1 lead to realistic variations of the ocean color for case 1 waters. Similar variations were observed for other D–P mixtures; i.e., the relative difference in A_{blk} was (much) less than 10% if m_{plk} was changed to 1.06 and/or m_{det} to 1.20 provided that we use Eq. (26) to constrain γ_{hyd} and that we preserve the values of q_p in Table 2. Because the intensity of linearly polarized light is a fixed percentage of these scattering functions for the D–P and M–P mixtures, use of these models for underwater light scattering computations lead also to realistic upper and lower bounds for water-leaving polarized radiance, respectively.

C. Top-of-the-Atmosphere Reflectance for Total and Polarized Water-Leaving Radiance Distributions

Figures 10 and 11 explore the bidirectional properties of water-leaving radiances for four ocean color cases of Fig. 8(b), namely, the D–P and M–P mixtures for [Chl] = 0.1 and 1.0 mg/m^3. We remark first that the TOA reflectance for these radiances is given by

$$\hat{I}_{rs} = \frac{\pi \tilde{I}_{rs}}{\mu_0 S_0}, \tag{30}$$

where S_0 is the extraterrestrial solar flux, and subscript rs stands for TOA remote sensing of radiance emerging from the bulk ocean system. Hence, $\tilde{\mathbf{I}}_{rs}$ is the underwater light contribution to the radiance vector obtained from reflection matrix $\mathbf{R}$ in Eq. (24). The linearly polarized reflectance for this contribution is given by

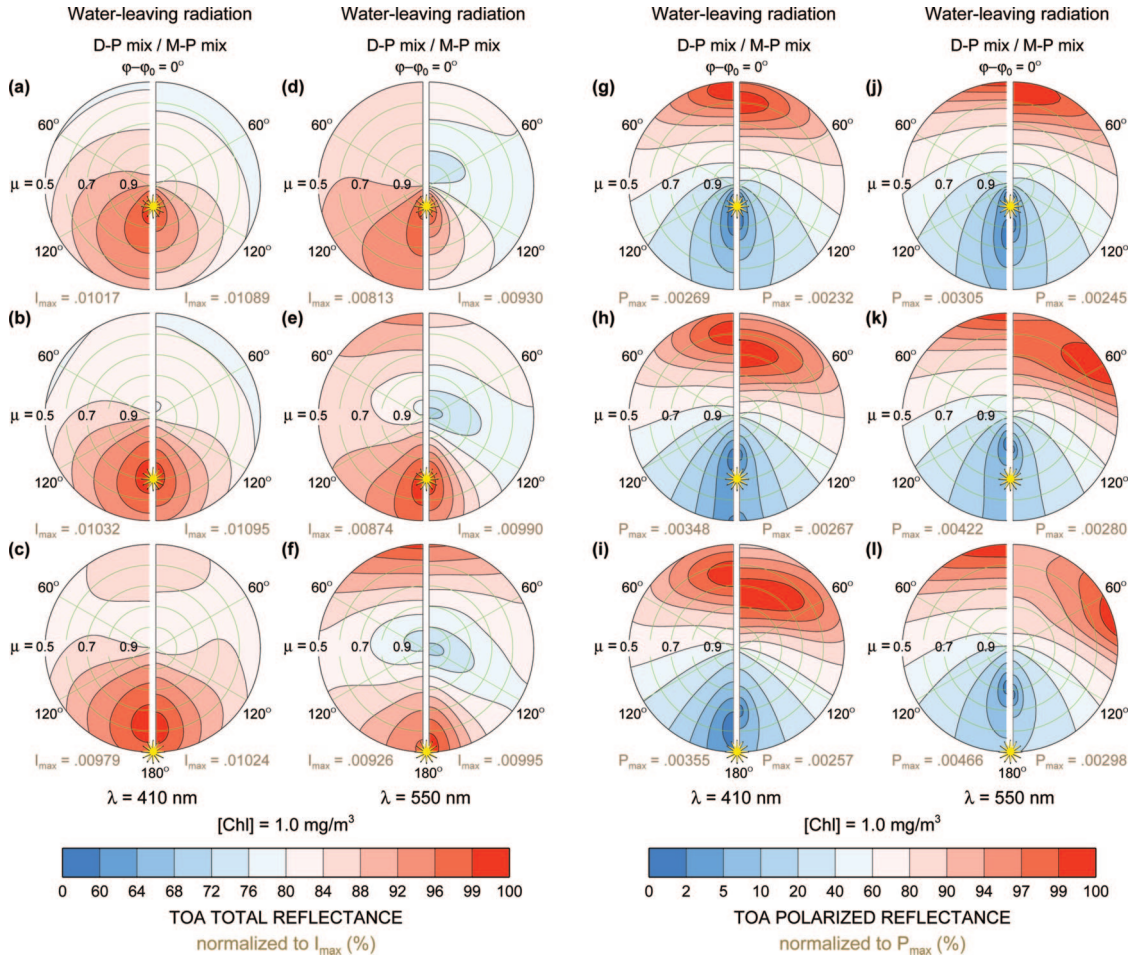

Fig. 11. Same as Fig. 10 except for [Chl] = 1.0 mg/m^3.

$$\hat{P}_{\mathrm{rs}} = \frac{\pi \tilde{P}_{\mathrm{rs}}}{\mu_0 S_0} = \frac{\pi \sqrt{\tilde{Q}_{\mathrm{rs}}^{\,2} + \tilde{U}_{\mathrm{rs}}^{\,2}}}{\mu_0 S_0}. \tag{31}$$

The reflectances in Eqs. (30) and (31) vary with the Sun and viewing angles, but they can also change by several factors in magnitude if [Chl] changes from 0.1 to 1.0 mg/m^3 and/or if the wavelength changes from blue to red (see the corresponding ocean albedos in Fig. 8). To compensate for such changes, we examine instead the bidirectional values of these reflectances defined as

$$\bar{I}_{\mathrm{rs}} = \frac{\hat{I}_{\mathrm{rs}}}{\max(\hat{I}_{\mathrm{rs}})} \equiv \frac{\hat{I}_{\mathrm{rs}}}{I_{\max}}, \tag{32}$$

$$\bar{P}_{\mathrm{rs}} = \frac{\hat{P}_{\mathrm{rs}}}{\max(\hat{P}_{\mathrm{rs}})} \equiv \frac{\hat{P}_{\mathrm{rs}}}{P_{\max}}, \tag{33}$$

respectively, where $\max(x)$ is the maximum of reflectance x for given range of viewing geometries. The study of these reflectances relative to the reflectance of the Earth depends on the highly variable properties of acrosols, which is beyond the scope of this work and reserved for a future paper. We will further refer to Eqs. (30) and to (31) as the reflectance of $\bar{I}_{\mathrm{rs}}$ and of $\bar{P}_{\mathrm{rs}}$, respectively. The left two columns of Figs. 10 and 11 show the polar diagrams of $\bar{I}_{\mathrm{rs}}$, and the right two columns show the polar diagrams of $\bar{P}_{\mathrm{rs}}$. The center point and circumference of each diagram correspond to viewing angle $\theta = 0°$ ($\mu = 1$) and $60°$ ($\mu = 0.5$), respectively, the latter of which is the largest viewing angle for the RSP instrument. A yellow star locates the antisolar position of the Sun, which varies between $\mu_0 = 0.9$ (first row), 0.7 (second row), and 0.5 (third row). The wavelength λ is 410 nm in the first and third columns, and 550 nm in the second and fourth columns. The value of [Chl] is 0.1 mg/m^3 in Fig. 10, and 1.0 mg/m^3 in Fig. 11. Each polar diagram is further divided into a left- and right-hand side hemisphere for D–P and M–P mixture results, respectively. The bidirectional values in each hemisphere are computed for 26 viewing angles $\times$ 90 azimuth angles = 2340 viewing geometries. The corresponding values for $I_{\max}$ are given below each hemisphere in the left two columns, and the same for $P_{\max}$ in the right two columns.

1. Total Reflectance at $\lambda = 410$ nm for [Chl] = 0.1 mg/m^3

From the first column in Fig. 10 we observe for $\lambda = 410$ nm and [Chl] = 0.1 mg/m^3 that $\bar{I}_{rs}$ is largest in the $\varphi - \varphi_0 = 180°$ half-plane at a viewing angle that varies with (but does not necessarily align with) the Sun angle, and that $\bar{I}_{rs}$ decreases from this maximum with decreasing azimuth angle down to about 75% in the $\varphi - \varphi_0 = 0°$ half-plane at $\mu = 0.5$. Comparison between the left- and right-hand side hemispheres shows further that replacing the D–P mixture with the M–P mixture causes the maximum reflectance and bidirectional values of $\bar{I}_{rs}$ to change by less than 3%. The fact that the $\bar{I}_{rs}$ maxima do not always occur in the backscaftering direction, and that the reflectance of these maxima does not vary much with F_{blk}, implies that they cannot simply be attributed to the glory of underwater light for direct (defined as attenuated but not scattered by the atmosphere) sunlight illumination of the ocean. Rather, one has to consider also

(i) the increase in atmospheric attenuation with decreasing μ_0 and μ, and

(ii) the increase in ocean surface reflection with decreasing μ_0 and μ.

These AOS properties follow from the optical path length for the atmosphere being equal to the product of its optical thickness with μ_0^{-1} for downwelling sunlight and with μ^{-1} for upwelling diffuse light,[1] and from the Fresnel coefficients for reflection,[100] respectively. Both the ocean surface reflection and atmospheric attenuation reduce the reflectance of $\bar{I}_{rs}$ for underwater light originating from direct sunlight illumination of the ocean. The decrease caused by AOS property (ii) in this reflectance is less than 15% if, as in Figs. 10 and 11, μ_0 and μ remain larger than 0.5. The decrease caused by AOS property (i) varies, however, for a molecular atmosphere at $\lambda = 410$ nm from a factor of slightly less than 2 for $\mu_0 = \mu = 1$, to more than 3 for $\mu_0 = \mu = 0.5$. The large attenuation factors of such an atmosphere, and the variation of these factors with scattering geometry, cause the maximum of this reflectance to appear at viewing angles that are closer to the nadir direction than the backscattering direction. The change in viewing angle is large for the D–P mixture (up to more than 20° for $\mu_0 \geq 0.5$), and slightly less for the M–P mixture because of the large underwater light glory for this mixture. The attenuation factors cause also the bidirectional values of this reflectance to decrease toward the horizon by up to 40% for both ocean mixtures.

Because the attenuation occurs by means of atmospheric scattering rather than by absorption, one has to consider for this wavelength also the reflectance of $\bar{I}_{rs}$ for underwater light originating from diffuse skylight illumination of the ocean. Computations show that the reflectance of this contribution exhibits a minimum in the $\varphi - \varphi_0 = 0°$ half-plane close to the nadir direction, and that it gradually increases with increasing azimuth angle to a maximum in the $\varphi - \varphi_0 = 180°$ half-plane at $\mu = 0.5$. The azimuthal change of this reflectance is therefore similar to the one for the reflectance originating from direct sunlight illumination. However, the magnitude of the former reflectance increases with moderate-to-large viewing angles as opposed to the magnitude of the latter reflectance, and the two reflectance fields become comparable for $\mu_0 = \mu = 0.5$. Furthermore, the former reflectance is especially for $\varphi - \varphi_0 > 120°$ less sensitive to the difference in F_{blk} between D–P and M–P mixtures than the latter reflectance. Hence adding the reflectance for underwater light originating from diffuse skylight illumination counters the rapid decrease of $\bar{I}_{rs}$ toward the horizon. It also causes the maximum reflectance of $\bar{I}_{rs}$ to increase by up to 80%, to be less sensitive to the hydrosol mixture, and to move several degrees back toward the backscattering direction.

2. Total Reflectance at $\lambda = 550$ nm for [Chl] = 0.1 mg/m^3

The variations of $\bar{I}_{rs}$ shown in the second column in Fig. 10 for $\lambda = 550$ nm are similar to those at $\lambda = 410$ nm for [Chl] = 0.1 mg/m^3. That is, there is a distinct maximum in the $\varphi - \varphi_0 = 180°$ half-plane from which $\bar{I}_{rs}$ decrease with decreasing azimuth angle down to a minimum in the $\varphi - \varphi = 0°$ half-plane. The differences are that this maximum occurs by up to 10° closer to the backscattering direction and that the reflectance of this maximum decreases 75%–80% (70%–75%) for the D–P (M–P) mixture. We note also that replacing the D–P mixture with the M–P mixture leads for $\lambda = 550$ nm to changes by up to about 15% for both the maximum reflectance and bidirectional values of $\bar{I}_{rs}$. The resulting change in $\bar{I}_{rs}$ between $\lambda = 410$ and 550 nm can be more than 10% (15%) near the nadir direction for the D–P (M–P) mixture. The causes for these changes are

(iii) the increase in ratio $b_p/(b_w + b_p)$ with increasing wavelength;

(iv) the decrease in single scattering albedo ω_{blk} with increasing wavelength; and

(v) the decrease in atmospheric attenuation with increasing wavelength.

AOS properties (iii) and (iv) derive among others from the moderate spectral decrease in b_p [i.e., λ^{-1} according to Eq. (11)] and from the strong spectral decrease in b_w (i.e., $\lambda^{-4.3}$ from Morel[54]). They lead to the increase of the fraction of light scattered by particulate matter [see Eq. (18)], and to the reduction of the order of underwater light scattering $(1 - \omega_{blk})^{-1}$ (see Morel and Gentili[34]), respectively. AOS property (v) follows from the molecular optical depth for the Earth's atmosphere being proportional[1] to λ^{-4}, and reduces the irradiance of diffuse skylight just above the ocean by a factor of up to 3. It also increases the irradiance of direct sunlight illumination of the ocean by 30% to 60% for $\mu_0 \geq 0.5$.

AOS property (v) implies that the reflectance of $\bar{I}_{rs}$ originating from diffuse skylight illumination is of secondary importance at $\lambda = 550$ nm. Consider therefore the reflectance of $\bar{I}_{rs}$ originating from direct sunlight illumination. Sensitivity studies show that both AOS properties (iii) and (iv) cause the maximum of this reflectance to decrease by a total of 80% to 85%. However, the studies show opposite trends for the bidirectional values of this reflectance, i.e., the values increase in case of AOS property (iii) and decrease in case of AOS property (iv) for $\varphi - \varphi_0 \leq 90°$ and μ_0, $\mu \leq 0.7$. The former change in these values is of the same order of magnitude as the latter change if λ changes from 410 to 550 nm and [Chl] = 0.1 mg/m^3, i.e., they tend to compensate one another for these λ and [Chl] values. Analyses performed for the D–P mixture confirm that the bidirectional values of this reflectance change for these scattering geometries by less than 4% for the sum of AOS properties (iii) and (iv). In fact, one can derive the spectral variation of $\bar{I}_{rs}$ in Fig. 10 for this mixture to within 6% for all angles by isolating the reflectance of $\bar{I}_{rs}$ originating from direct sunlight illumination of the ocean, and by decreasing the atmospheric attenuation of direct light conform a change in λ from 410 to 550 nm [AOS property (v)]. Analyses performed for the M–P mixture show that the change in $\bar{I}_{rs}$ by AOS property (iii) is larger for viewing geometries corresponding to the range of underwater light single scattering angle Θ between 130° and 170°, and slightly smaller for the other geometries. Note that F_p is smaller for the M–P mixture than for the D–P mixture for this range of Θ when normalized by the glory (see Fig. 4), and that AOS property (iii) causes F_{blk} to be more sensitive to this difference in F_p. The net change in $\bar{I}_{rs}$ by the sum of AOS properties (iii) and (iv) varies therefore also with the shape of F_p. For the M–P mixture and direct sunlight illumination, it can be up to 15% for viewing geometries corresponding to $130° \leq \Theta \leq 170°$ and up to 10% for the other geometries, which cannot be ignored in the spectral variation of $\bar{I}_{rs}$ in Fig. 10.

3. Polarized Reflectance at $\lambda = 410$ nm for [Chl] = 0.1 mg/m^3

The third column of Fig. 10 shows for $\lambda = 410$ nm and [Chl] = 0.1 mg/m^3 very different patterns for the polarized component of $\bar{I}_{rs}$. We observe first that $\bar{P}_{rs}$ is largest in the $\varphi - \varphi_0 = 0°$ half-plane, where it remains for various sun angles close to but not at $\mu = 0.5$ for the D–P mixture. Second, $\bar{P}_{rs}$ decreases with increasing azimuth angle down to one or more minima of less than 2% in the $\varphi - \varphi_0 = 180°$ half-plane. Third, replacing the D–P with the M–P mixture moves the maximum of $\bar{P}_{rs}$ by up to 5° toward the nadir direction, and increases $\bar{P}_{rs}$ by up to over 10% for $\varphi - \varphi_0 \approx 90°$. It also causes the maximum reflectance of $\bar{P}_{rs}$ to decrease by about 10% for $\mu_0 = 0.9$ to almost 20% for $\mu_0 = 0.5$. These observations are, to a first approximation, consistent with the polarization of underwater light single scattering for unidirectional, unpolarized incident light. Note that the reflectance of this polarization is proportional to the product $p_{blk} \times F_{blk}$. The observations differ, however, from this approximation in the lack of a polarization minimum in the backscattering direction, where p_{blk} is zero, and in the occurrence of a polarization maximum at $\mu > 0.5$, where $p_{blk} \times F_{blk}$ is not largest. The former difference can partially be attributed to the multiple scattering of underwater light and the latter one to the decrease in atmospheric transmission of this light by AOS property (i). However, one should also consider

(vi) the change with μ and μ_0 of polarization by ocean surface transmission.

This AOS property follows from the Fresnel coefficients for refraction,[100] and causes the ocean body just below the surface to be illuminated by a linearly polarized, rather than by an unpolarized, light field for direct incident sunlight. The degree of polarization for this field increases with incident angle up to 30%.[101] Furthermore, its direction of polarization is perpendicular to the one for single scattering by hydrosols. This modifies the polarized reflectance of underwater light scattering for direct incident sunlight, and changes it again upon transmission back to the atmosphere by the ocean surface. The largest changes occur in the principal plane (i.e., plane containing the $\varphi - \varphi_0 = 0°$ and $\varphi - \varphi_0 = 180°$ half-planes) where they lead to a decrease in this reflectance throughout the $\varphi - \varphi_0 = 0°$ half-plane except for $\mu \approx 1$, and to an increase in the $\varphi - \varphi_0 = 180°$ half-plane around the backscattering direction. The former decrease in reflectance causes of the maximum of this reflectance to appear at smaller viewing angles and in case of the M–P mixture and $\mu_0 = 0.5$, even outside the $\varphi - \varphi_0 = 0°$ half-plane because of the small gradient of $p_{blk} \times F_{blk}$ at sideward-scattering angles for this mixture (see also $\bar{P}_{rs}$ at $\lambda = 550$ nm). The increase in reflectance for $\varphi - \varphi_0 = 180°$ causes the minima of this reflectance to move in the principal plane away from the backscattering direction, and is accompanied by a rotation of 90° in the direction of polarization along this move.

In addition, one has to consider the reflectance of $\bar{P}_{rs}$ for underwater light originating from diffuse skylight illumination. Computations show that this reflectance exhibits a maximum in the $\varphi - \varphi_0 = 0°$ half-plane at $\mu_0 = 0.5$, and a minimum outside the $\varphi - \varphi_0 = 180°$ half-plane at viewing angles that follow the sun. The changes caused by AOS property (vi) in this reflectance are again largest in the principal plane, but they amount to a decrease in reflectance in both the $\varphi - \varphi_0 = 0°$ and $\varphi - \varphi_0 = 180°$ half-planes except for $\mu \approx 1$. The change in the $\varphi - \varphi_0 = 0°$ half-plane causes the maximum of this reflectance to appear at smaller viewing angles for $\mu_0 = 0.5$, but it does not increase the azimuth angle of this maximum even for the M–P mixture. The reflectance decrease

in the $\varphi - \varphi_0 = 180°$ half-plane causes the minima of this reflectance to appear at larger azimuth and viewing angles, but it does not rotate the direction of polarization along this half-plane.

The resulting differences between the reflectances of $\bar{P}_{rs}$ originating from direct sunlight and from diffuse skylight illumination are as follows. Results obtained for $\varphi - \varphi_0 \leq 90°$ show that both reflectances differ by less than 10° in the direction of polarization, but that the reflectance originating from diffuse skylight illumination is between 1.5 to 3 times smaller in magnitude than the one originating from direct sunlight illumination. Adding the latter reflectance to the former one increases therefore the reflectance of $\bar{P}_{rs}$ for this azimuth range, but it changes the corresponding bidirectionality only by several percent for the M–P mixture and less for the D–P mixture. Results obtained for $\varphi - \varphi_0 > 120°$ show, on the other hand, that the directions of polarization for these reflectances can become mutually perpendicular in the $\varphi - \varphi_0 = 180°$ half-plane, and that the latter reflectance can become comparable to the former reflectance. The sum of these reflectances causes the minima of the former reflectance to move substantially toward the backscattering direction, and the magnitude of the former reflectance to reduce between these minima by a factor of up to 2 for the M–P mixture and up to 3 for the D–P mixture.

4. *Polarized Reflectance at $\lambda = 550$ nm for [Chl] = 0.1 mg/m^3*

The results for $\bar{P}_{rs}$ at $\lambda = 550$ nm in the fourth column of Fig. 10 show remarkable changes from $\lambda = 410$ nm in case of the M–P mixture. That is, the polarization maximum for this ocean mixture resides now at azimuth angles larger than 60° if $\mu_0 \leq 0.7$, which causes $\bar{P}_{rs}$ to differ between the two ocean mixtures by up to more than 25% for $\varphi - \varphi_0 \approx 90°$. The reflectance of this maximum also decreases more than 25% from the maximum for the D–P mixture if $\mu_0 = 0.5$. In addition, we observe for both ocean mixtures the viewing angle for this maximum to increase by up to 15°, the reflectance of this maximum to decrease by 65% to 70%, and the viewing angles of the polarization minima to vary by up to more than 5°. The resulting spectral change in $\bar{P}_{rs}$ can be more than 15% near the nadir direction in case of the D–P mixture, and up to 15% near $\mu = 0.5$ for $\varphi - \varphi_0 \approx 90°$ in case of the M–P mixture. Note that the Fresnel coefficients for the ocean surface do not change much in the visible part of the spectrum which means that AOS property (vi) is virtually constant between $\lambda = 410$ and 550 nm. The spectral changes seen in Fig. 10 for $\bar{P}_{rs}$ must therefore originate from changes in the reflectance contributions to $\bar{P}_{rs}$ with AOS properties (iii), (iv), and (v). Computations for the reflectance of $\bar{P}_{rs}$ originating from direct sunlight illumination of the ocean show that the maximum of this reflectance is particularly sensitive to AOS properties (iii) and (v). The latter property causes this maximum to not only move toward substantially larger viewing angles, but because of the change in polarization by ocean surface transmission [AOS property (vi)] to also appear outside the $\varphi - \varphi_0 = 0°$ half-plane if $\mu_0 \leq 0.5$ (0.7) for the D–P (M–P) mixture. AOS property (iii), on the other hand, increases the gradient of $p_{blk} \times F_{blk}$ at sideward-scattering angles for the D–P mixture and decreases it for the M–P mixture, which causes this maximum to move back to and further from the $\varphi - \varphi_0 = 0°$ half-plane, respectively. Both AOS properties (iii) and (iv) further cause the minima for this $\bar{P}_{rs}$ to move toward the backscattering direction. The change in viewing angle for these minima amounts is slightly larger for AOS property (iii) and for the M–P ocean mixture, and is accompanied by a rotation of 90° in the direction of polarization.

Computations for the maximum and minima of $\bar{P}_{rs}$ for underwater light originating from diffuse skylight illumination show similar angular sensitivities to AOS properties (iii)–(v) except that the maximum remains within the $\varphi - \varphi_0 = 0°$ half-plane for the D–P mixture in case of AOS property (v), and that the minima move away from the $\varphi - \varphi_0 = 180°$ half-plane in case of AOS properties (iii) and (iv). They further show a decrease by more than 90% in the reflectance of this maximum as result of AOS properties (iii), (iv), and (v). The maximum reflectance of $\bar{P}_{rs}$ originating from direct sunlight illumination decreases also (by close to 80% with AOS properties (iii) and (iv); however, it increases with AOS property (v) such that its magnitude becomes more than sevenfold the reflectance maximum from diffuse skylight illumination. This causes the contribution from diffuse skylight illumination to change the reflectance and bidirectional values of $\bar{P}_{rs}$ by less than 15% and 2%, respectively, if $\varphi - \varphi_0 \leq 90°$. The corresponding changes for $\varphi - \varphi_0 \geq 120°$ are larger especially in the $\varphi - \varphi_0 = 180°$ half-plane because the reflectance contributions to $\bar{P}_{rs}$ differ there by a factor of (much) less than 7, and because the directions of polarization can there be mutually perpendicular. Still, the contribution from diffuse skylight illumination causes the reflectance values of $\bar{P}_{rs}$ to decrease there by less than 50% for the D–P mixture and 20% for the M–P mixture, and the minima of $\bar{P}_{rs}$ to move by only a couple degrees for both ocean mixtures.

5. *Total Reflectance at $\lambda = 410$ and 550 nm for [Chl] = 1.0 mg/m^3*

Changing [Chl] from 0.1 in Fig. 10 to 1.0 mg/m^3 in Fig. 11 affects the bidirectionality and reflectance of $\bar{I}_{rs}$ as follows. From the first columns of these figures, we derive for $\lambda = 410$ nm that for both ocean mixtures the maximum of $\bar{I}_{rs}$ occurs a few degrees closer to the backscattering direction for $\mu_0 \leq 0.7$, that the reflectance of this maximum decreases 55%–60%, and that $\bar{I}_{rs}$ exhibits the emergence of a second maximum in $\varphi - \varphi_0 = 0°$ half-plane. The difference in maximum reflectance and bidirectional values of $\bar{I}_{rs}$

between the two mixtures is about 6% or less for [Chl] = 1.0 mg/m^3 and λ = 410 nm. However, the appearance of the second maximum for this [Chl] value causes the variation of $\bar{I}_{rs}$ with [Chl] to be larger; i.e., it approaches for λ = 410 nm up to 15% for both ocean mixtures. From the second columns of these figures, we derive for $\bar{I}_{rs}$ at λ = 550 nm that the change with [Chl] in $\bar{I}_{rs}$ can now amount up to 25% for the D–P mixture and up to 30% for the M–P mixture. The corresponding change in maximum reflectance of $\bar{I}_{rs}$ is an increase by 55%–65% (50%–60%) for the D–P (M–P) mixture. However, the differences in this reflectance or in the bidirectional values of $\bar{I}_{rs}$ when replacing the D–P by the M–P mixture remain less than 15% for [Chl] = 1.0 mg/m^3 and λ = 550 nm. Changing [Chl] causes the largest variations in $\bar{I}_{rs}$ especially if λ = 550 nm. The causes for these variations are

(vii) the decrease in detritus fraction f_{det} with increasing [Chl];
(viii) the increase in ratio $b_p/(b_w + b_p)$ with increasing [Chl]; and
(ix) the increase in single scattering albedo ω_{blk} with increasing [Chl].

AOS property (vii) is the relation in Eq. (28) derived from the change in q_p with [Chl], and AOS properties (viii) and (ix) follow from the increase with [Chl] of b_p in Eq. (11). The former two AOS properties increase the fraction of light scattered by in particular plankton particles [see Eqs. (18) and (22)], and computations show this to cause a decrease in the maximum reflectance of $\bar{I}_{rs}$ for both direct sunlight and diffuse skylight illumination between 65% and 70% at λ = 410 nm if [Chl] changes from 0.1 to 1.0 mg/m^3. The corresponding decrease for λ = 550 nm is between 55% and 65%. AOS property (ix), on the other hand, raises the order of underwater light scattering [see discussion on AOS property (iv)]. The raise at λ = 410 nm is moderate (30%) if [Chl] changes from 0.1 to 1.0 mg/m^3, but it almost triples at λ = 550 nm for the same range of [Chl]. Calculations for the maximum reflectance of $\bar{I}_{rs}$ show a corresponding increase for both direct sunlight and diffuse skylight illumination by about 30% for λ = 410 nm, and by a factor between 3.5 and 4 for λ = 550 nm.

The differences between Figs. 10 and 11 in bidirectional values of $\bar{I}_{rs}$ derive mostly from the changes with AOS properties (viii) and (ix) of the reflectance of $\bar{I}_{rs}$ originating from direct sunlight illumination. Computations performed for λ = 410 nm show that AOS property (viii) causes the maximum of this reflectance to appear closer to the backscattering direction by up to more than (less than) 5° for the M–P (D–P) mixture. AOS property (viii) also increases the bidirectional values of this reflectance for $\varphi - \varphi_0 \leq 90°$ and $\mu_0 \leq 0.7$ by up to (slightly less than) 20% for the D–P (M–P) mixture. AOS properties (vii) and (ix), respectively, reduce and enhance the change in bidirectional values by less than 5%; i.e., their effect on these values tend to cancel each other for λ = 410 nm. In fact, most of the changes in $\bar{I}_{rs}$ between Figs. 10 and 11 can for λ = 410 nm be reproduced to within 1% (2%) for the D–P (M–P) mixture simply by increasing the ratio $b_p/(b_w + b_p)$ conform AOS property (viii). The case for λ = 550 nm is somewhat different because of the large variation in ω_{blk} for this wavelength and range of [Chl]. In addition, the change with AOS property (viii) of $\bar{I}_{rs}$ for $\varphi - \varphi_0 \leq 90°$ and $\mu_0 \leq 0.7$ becomes now more complicated for the M–P mixture because of an increase in sensitivity to the shape of F_p [see discussion on AOS property (iii)]. Computations confirm that to approximate the change with [Chl] of $\bar{I}_{rs}$ for this wavelength well within 5%, one has to vary both ω_{blk} and $b_p/(b_w + b_p)$ conform AOS properties (viii) and (ix). They also show that, because of the small spectral variation of ω_{blk} for [Chl] = 1.0 mg/m^3, one can still derive the spectral change of $\bar{I}_{rs}$ for [Chl] = 1.0 mg/m^3 to within 6% (8%) for the D–P (M–P) mixture if AOS property (iv) is ignored.

6. *Polarized Reflectance at λ = 410 and 550 nm for [Chl] = 1.0 mg/m^3*

The reflectance and bidirectional values of $\bar{P}_{rs}$ exhibit each a different sensitivity to a change in [Chl] from 0.1 to 1.0 mg/m^3. That is, from the third columns of Figs. 10 and 11 we derive for λ = 410 nm that the maxima of $\bar{P}_{rs}$ vary up to a few degrees in viewing angle, that the reflectances of these maxima decrease 50%–55% (55%–60%) for the D–P (M–P) ocean mixture, and that the minima of $\bar{P}_{rs}$ can move up to 5° toward the backscattering direction. We observe also for the D–P mixture a substantial decrease in $\bar{P}_{rs}$ between its minima, and for the M–P mixture the appearance of its polarization maximum outside the principal plane for μ_0 = 0.5. As a result, the difference in bidirectional values of $\bar{P}_{rs}$ between the two mixtures can now reach up to about 15% for $\varphi - \varphi_0 \approx 90°$ if [Chl] = 1.0 mg/m^3 and λ = 410 nm. The corresponding change in maximum reflectance is also large, i.e., a decrease from almost 15% for μ_0 = 0.9 to almost 30% for μ_0 = 0.5. Nevertheless, the change with [Chl] in $\bar{P}_{rs}$ is only about 5% or less for both ocean mixtures if λ = 410 nm. Comparisons between the fourth columns of Figs. 10 and 11 show the angular features of $\bar{P}_{rs}$ to be less sensitive to [Chl] if λ = 550 nm. Consequently, changing [Chl] from 0.1 to 1.0 mg/m^3 causes $\bar{P}_{rs}$ at this wavelength to vary even less than 5% for both ocean mixtures. Also, replacing the D–P by the M–P mixture leads at λ = 550 nm to changes in $\bar{P}_{rs}$ that remain similarly large (i.e., up to ~25%) for [Chl] = 0.1 and 1.0 mg/m^3. Still, the maximum reflectance of $\bar{P}_{rs}$ increases 70%–80% (50%–60%) with [Chl] for the D–P (M–P) mixture if λ = 550 nm. And switching the D–P with the M–P mixture at [Chl] = 1.0 mg/m^3 and λ = 550 nm causes this reflectance to decrease around

20%(35%) for $\mu_0 = 0.9\,(0.5)$, i.e., more than at $\lambda = 410$ nm.

To dissect the changes in $\bar{P}_{rs}$ between Figs. 10 and 11, we proceed by examining the variations in the contributions to $\bar{P}_{rs}$ with AOS properties (vii), (viiii), and (ix). Note that AOS property (viii) causes the gradient of $p_{blk} \times F_{blk}$ to increase (decrease) for the D–P (M–P) mixture in the same fashion as AOS property (iii) does. However, single scattering analyses show that this change is partially compensated by an opposing change with AOS property (vii). Computations for direct sunlight illumination of the ocean confirm that AOS property (viii) causes the maximum of $\bar{P}_{rs}$ for the two ocean mixtures to move in opposite directions in the $\varphi - \varphi_0 = 0°$ half-plane, and for the M–P mixture to move away from this half-plane similar to the case of AOS property (iii). They also show that the largest angular changes occur for the maximum of the M–P mixture at $\lambda = 410$ nm, and that these changes are reduced by more than half when including AOS property (vii). The corresponding results for $\varphi - \varphi_0 > 90°$ are that AOS property (viii) causes the minima of $\bar{P}_{rs}$ to move toward the backscattering direction, and that changes in viewing angle for these minima are largest for the M–P mixture and/or $\lambda = 410$ nm, come with a rotation of 90° in the direction of polarization, and are rather insensitive to AOS property (vii). Including AOS property (ix) in these computations causes the polar angles of the $\bar{P}_{rs}$ maxima and minima to change by ~2° or less for both ocean mixtures if $\lambda = 410$ nm. The corresponding changes for $\lambda = 550$ nm can be much larger; however, they tend to cancel the changes incurred by the sum of AOS properties (vii) and (viii) for this wavelength.

Polar angle computations for the maxima and minima of $\bar{P}_{rs}$ originating from diffuse skylight illumination show similar changes with AOS properties (vii)–(ix) except that the M–P maxima move further from the $\varphi - \varphi_0 = 0°$ half-plane in case of AOS property (ix) at 550 nm. The exceptions for the minima of $\bar{P}_{rs}$ are that they move away from the $\varphi - \varphi_0 = 180°$ half-plane, and that the changes are occasionally larger for the D–P than for the M–P mixture. Reflectance computations for $\bar{P}_{rs}$ show a decrease in maximum with AOS properties (vii) and (viii) by about 60% to 70% at $\lambda = 410$ nm, and by 50% to 60% at $\lambda = 550$ nm, if [Chl] changes from 0.1 to 1.0 mg/m^3. The decrease is slightly larger for diffuse skylight illumination than for direct sunlight illumination of the ocean, which causes the ratio of the corresponding reflectances for $\bar{P}_{rs}$ to drop if $\varphi - \varphi_0 \leq 90°$. On the other hand, the ratio of these reflectances increases around the backscattering direction because of the changes in their minima discussed above. The reflectance ratio becomes there closest to unity—and the sum of its reflectances therefore closest to zero—for $\lambda = 410$ nm and the D–P mixture. It remains, however, below 0.3 for either ocean mixture if $\lambda = 550$ nm, and is further not very sensitive to AOS property (ix). The computations show further AOS property (ix) to increase the maximum reflectance of $\bar{P}_{rs}$ by 20% to 25% at 410 nm, and by a factor of 3 to 3.5 at 550 nm.

4. Summary

The present work provides a hydrosol model for use in underwater light scattering computations to study variations in the reflectance for total and polarized water-leaving radiances observed from space. The model consists of two components whose refractive indices resemble those of detrituslike and planktonlike particles, whose size distributions are constrained by underwater light linear polarization signatures, and whose mixing ratios are set by user-defined backscattering efficiencies. The latter efficiencies are given by bio-optical relations for case 1 (open ocean) waters as a function of chlorophyll *a* concentration [Chl], but they can also be taken from field measurements. The underwater light linear polarization signatures are bounded by the one for pure water. The advantages of such so-called D–P mixtures are that their microphysical properties are consistent with *in situ* measurements of oceanic particulates, that the resulting scattering function can be made dependent on the chlorophyll *a* pigment concentration [Chl] and on the wavelength λ as is commonly assumed for case 1 waters, and that the polarization of light scattered by such mixtures constitutes an upper bound for real observations. They do not address, however, the uncertainty in glory of hydrosol scattering functions, and may on occasion lead to an overestimate of the underwater light polarization. To examine variations in the reflectance for total and polarized water-leaving radiances resulting from such uncertainties, a second hydrosol model is provided consisting of a mixture of detrituslike particles and mineralike particles. These so-called M–P mixtures possess the same particles backscattering efficiencies as the D–P mixtures, but the glory is significantly different for the scattering functions of these mixtures. It is also the case that the polarization of light scattered by the M–P mixtures is lower than actually observed for sideward-scattering in the open ocean, and that it exhibits a small but unusual second maximum closer to the backscattering direction.

Multiple scattering computations performed for case 1 waters and a molecular atmosphere show that both the D–P and M–P mixtures lead to realistic variations with [Chl] and λ in the ocean body albedo (A_{blk}) just below the surface for $0.03 \text{ mg/m}^3 \leq$ [Chl] $\leq 3.0 \text{ mg/m}^3$ and for $400 \text{ nm} \leq \lambda \leq 600$ nm. They also show that the TOA maximum reflectance I_{max} for water-leaving radiances follows these variations to a significant degree. That is, $I_{max}\,(A_{blk})$ decreases by 55%–60% (60%–65%) at $\lambda = 410$ nm, and increases by 55%–65% (70%–90%) at $\lambda = 550$ nm, for $\mu, \mu_0 \geq 0.5$ if [Chl] varies from 0.1 mg/m^3 to 1.0 mg/m^3 in a case 1 ocean containing D–P mixtures. The corresponding change in I_{max} for a case 1 ocean containing M–P mixtures is slightly smaller (50%–60%) if

λ=550 nm. The results for the maximum polarized reflectance P_{max} for remotely sensed water-leaving radiances exhibit the same decrease (55%–60%) at λ = 410 nm, and the same increase (50%–60%) at λ=550 nm, as I_{max} for this range of [Chl] in a case 1 ocean containing M–P mixtures. The change with [Chl] in P_{max} for λ = 410 is also similar (i.e., a decrease of 50%–55%) to the one for I_{max} if the ocean contains D–P mixtures. However, it becomes significantly larger for such an ocean if λ = 550 nm, i.e., P_{max} increases then by 70%–80%. Replacing a D–P by a M–P mixture at [Chl] = 0.1 or 1.0 mg/m^3 causes I_{max} to vary less than 5% for λ = 410 nm, and by up to 15% for λ = 550 nm. The corresponding changes in P_{max} are much larger, i.e., from $\leq$20% for λ = 410 nm to $\leq$25% for λ = 550 nm at [Chl] = 0.1 mg/m^3, and from $\leq$30% for λ = 410 nm to $\leq$35% for λ= 550 nm at [Chl] = 1.0 mg/m^3.

The computations confirm further the bidirectional nature of the reflectance for total and polarized water-leaving radiances observed from space. Common features of $\bar{I}_{rs}$ include a maximum near or at the backscattering direction, and the emergence of a second maximum in the $\varphi - \varphi_0 = 0°$ half-plane for midvisible wavelengths λ and mesotrophic chlorophyll a concentrations [Chl]. The features of $\bar{P}_{rs}$ include the occurrence of one or more minima in the $\varphi - \varphi = 180°$ half-plane depending on the Sun angle, λ, and [Chl], and a rapid increase by more than an order of magnitude toward a maximum in the $\varphi - \varphi_0 \leq 90°$ azimuth range. Calculations show that the variation of $\bar{I}_{rs}$ with λ and with [Chl] depends on the reflectance contribution to $\bar{I}_{rs}$ originating from diffuse skylight and direct sunlight illumination of the ocean, on the variation of each of these contributions with the underwater light single scattering properties ω_{blk} and $\boldsymbol{F}_{blk}$, and on the variation of each of these properties with λ and [Chl]. The same holds for the reflectance contributions of $\bar{P}_{rs}$ except that their sum depends also on direction of polarization of each contribution, and that this direction may vary with ω_{blk}, $\boldsymbol{F}_{blk}$, and (not discussed in this paper) the polarization of skylight. The resulting change in $\bar{I}_{rs}$ can for μ, $\mu_0 \geq 0.5$ reach 15% at λ = 410 nm, and ~25% at λ = 550 nm, if [Chl] varies from 0.1 mg/m^3 to 1.0 mg/m^3 in a case 1 ocean with D–P hydrosol mixtures. The corresponding change in $\bar{P}_{rs}$ is much smaller, i.e., by ~5% or less for both λ = 410 and 550 nm. These upper bounds for changes in bidirectionality remain the same whether the ocean contains D–P mixtures or M–P mixtures. However, replacing a D–P by a M–P mixture for a given [Chl] causes $\bar{I}_{rs}$ to vary ~5% or less for λ = 410 nm, and $\leq$15% for λ = 550 nm. The corresponding variation in $\bar{P}_{rs}$ is much larger, i.e., from $\leq$15% for λ = 410 nm to $\leq$25% for λ = 550 nm.

There are a number of observations emerging from this study that are of interest to the aerosol and ocean color communities. First, they show that underwater light polarization data can provide useful relationships between the size distribution and refractive index of hydrosol particles. This is among others of interest in identifying the particulate sources of the backscattering coefficient s_{blk}, which is an ongoing field of research in underwater light studies.[102] Second, they explain why the reflectance for polarized water-leaving radiances becomes small (i.e., $\ll 10^{-3}$) in the $\varphi - \varphi_0 = 180°$ half-plane for a wide range of viewing angles on each side of the backscattering direction, and they show this to be occurring for a broad range of [Chl], λ, and hydrosol mixtures. This observation provides support for the method used by Chowdhary *et al.*[10,82] to retrieve aerosol properties over the ocean from polarized reflectances remotely sensed in the principal plane. Third, they reveal that while such reflectances become larger than 10^{-3} for $\varphi - \varphi_0 < 150°$, the corresponding bidirectionality changes very little with [Chl] for given wavelength and hydrosol mixture. Note that this bidirectionality can differ significantly from the one for polarized reflectance of an atmosphere that is bounded from below by an ocean surface. This implies that the polarimetric analyses by Chowdhary *et al.*[10,82] may be extended to off-principal plane viewing angles by scaling the polarized reflectance for water-leaving radiances of a reference ocean to fit TOA observations as a function of aerosol properties. The best-fit result leads not only to an aerosol retrieval but also to the spectrum of polarized water-leaving radiances, which provides an estimate of [Chl] and therefore a useful, additional constrain for the photometric color of the true ocean. The fourth observation emerging from this study is that the bidirectionality of polarized water-leaving radiance is quite sensitive to the mixture of hydrosols, or more precisely, to the uncertainty in the degree of underwater light linear polarization. The change in this bidirectionality with underwater light polarization is significant in this study because of our choice for the scattering properties of the D–P and M–P mixtures, but it also represents the maximum range to be expected for open oceans. One can therefore reduce the uncertainty in this bidirectionality by forcing the degree of bulk ocean underwater light linear polarization p_{blk} to reside between those of the D–P ($p_{blk} \leq 85\%$) and those of the M–P ($p_{blk} \leq 65\%$) ocean mixtures. Indeed, preliminary results show this to decrease the uncertainty in this bidirectionality to well below 5% (paper in preparation).

Appendix A: Notation

A_{fm}	Albedo of the ocean surface foam (dimensionless)
A_{blk}	Albedo of the bulk ocean body (dimensionless)
A_{bot}	Albedo of the ocean bottom (dimensionless)
a_p, a_w	Absorption coefficient for the particulate matter of ocean waters and for pure seawater, respectively (m^{-1})

b_p, b_w	Scattering coefficient for the particulate matter of ocean waters and for pure seawater, respectively (m^{-1})
[Chl]	Chlorophyll a concentration (mg m^{-3})
c_p	Extinction coefficient for the particulate matter of ocean waters (m^{-1})
$\Delta\tau_{blk}$	Bulk optical thickness of an oceanic layer (dimensionless)
$\Delta\tau_{mol,abs}$	Molecular absorption optical thickness of an atmospheric layer (dimensionless)
$\Delta\tau_{mol,sca}$	Molecular scattering optical thickness of an atmospheric layer (dimensionless)
$\Delta\tau_{aer,ext}$	Aerosol extinction optical thickness of an atmospheric layer (dimensionless)
δ_{mol}, δ_w	Depolarization factors for molecular scattering in the atmosphere and ocean body, respectively (dimensionless)
E_d, E_u	Downward and upward irradiance just below the ocean surface, respectively (W m^{-2})
$\mathbf{F}$	Scattering matrix of a volume element in the atmosphere–ocean system (4×4 matrix; dimensionless)
$\mathbf{F}_{blk}$	Bulk scattering matrix of an oceanic layer (4×4 matrix; dimensionless)
$\mathbf{F}_p$, $\mathbf{F}_w$	Particulate matter and pure seawater scattering matrix components of $\mathbf{F}_{blk}$, respectively (4×4 matrices; dimensionless)
$\mathbf{F}_{det}$, $\mathbf{F}_{mnr}$, $\mathbf{F}_{plk}$	Detritus, mineral, and plankton scattering matrix components of $\mathbf{F}_p$, respectively (4×4 matrices; dimensionless)
$\mathbf{F}_{hyd}$	Hydrosol scattering matrix $\mathbf{F}_{det}$, $\mathbf{F}_{mnr}$, or $\mathbf{F}_{plk}$ (4×4 matrix; dimensionless)
f_{det}, f_{mnr}	Fraction of particles that are detritus and mineral, respectively (dimensionless)
g_1, g_2	Asymmetry parameters of a two-term Henyey–Greenstein (TTGH) function (dimensionless)
g_p	Asymmetry parameter of a particulate matter scattering function consisting of a one-term Henyey–Greenstein function (dimensionless)
γ_{plk}, γ_{det}	Junge exponent for the size distributions of plankton and detritus particles, respectively (dimensionless)
γ_{hyd}	Junge exponent γ_{plk} or γ_{det} (dimensionless)
Θ	Single scattering angle (degrees)
θ	Zenith angle of the direction of light propagation, measured from the positive z axis (degrees)
$\mathbf{I}$	Stokes vector (4×1 matrix; W m^{-2} nm^{-1})
$\tilde{\mathbf{I}}$	Radiance vector (4×1 matrix; W m^{-2} nm^{-1} sr^{-1})
$\hat{\mathbf{I}}$	Reflectance vector (4×1 matrix; dimensionless)
I, Q, U, V,	First, second, third, and fourth parameter of $\mathbf{I}$(W m^{-2} nm^{-1})
$\tilde{I}$, $\tilde{Q}$, $\tilde{U}$, $\tilde{V}$,	First, second, third, and fourth parameter of $\tilde{\mathbf{I}}$ (W m^{-2} nm^{-1} sr^{-1})
$\tilde{I}_{rs}$	Radiance of water-leaving radiation at TOA (W m^{-2} nm^{-1} sr^{-1})
$\hat{I}$	Reflectance for water-leaving radiation at TOA (dimensionless)
$\bar{I}_{rs}$	Bidirectional values of $\hat{I}_{rs}$ (dimensionless)
I_{max}	Maximum value of $\hat{I}$ (dimensionless)
K_{blk}, K_w, K_{bio}	Diffuse attenuation coefficient for the bulk ocean and for its pure seawater and biogenic (particulate and dissolved) components, respectively (m^{-1})
$\mathbf{L}$	Matrix to rotate reference systems (4×4 matrix; dimensionless)
λ	Wavelength (nm)
m_{plk}, m_{det}, m_{mnr}	Complex refractive index of plankton, detritus, and mineral particles, respectively, relative to seawater (dimensionless)
m_{hyd}	Complex refractive index m_{plk}, m_{det}, or m_{mnr} (dimensionless)
m_{srf}	Complex refractive index of the ocean surface, relative to air (dimensionless)
μ	$\lvert u \rvert$ (dimensionless)
n_{hyd}	Differential particle size distribution of hydrosol particles (m^{-3})
P	Linearly polarized component of I (W m^{-2} nm^{-1})
$\tilde{P}_{rs}$	Linearly polarized component of $\tilde{I}_{rs}$ (W m^{-2} nm^{-1} sterad^{-1})
$\hat{P}_{rs}$	Linearly polarized component of $\hat{I}$ (dimensionless)
$\bar{P}_{rs}$	Bidirectional values of $\hat{P}_{rs}$ (dimensionless)
P_{max}	Maximum value of $\hat{P}_{rs}$ (dimensionless)
p_{hyd}, p_w, p_{blk}	Linear polarization percentage $-F_{21}/F_{11}$ of $\mathbf{F}_{hyd}$, $\mathbf{F}_w$, and $\mathbf{F}_{blk}$, respectively (%)
q_p	Backscattering efficiency of F_p (dimensionless)

q_{det}, q_{mnr}, q_{plk}	Backscattering efficiencies of F_{det}, F_{mnr}, and F_{plk}, respectively (dimensionless)
$\mathbf{R}$	Atmosphere–ocean system reflection matrix (4×4 matrix; dimensionless)
r	Radius of hydrosol particle (μm)
r_{eff}	Effective radius of hydrosol size distribution (μm)
s_{blk}	backscattering coefficient of bulk oceanic water (m^{-1})
σ_{det}, σ_{mnr}, σ_{plk}	Scattering cross sections of detritus, mineral, and plankton particles, respectively ($\mu\mathrm{m}^2$)
τ	Optical depth in the atmosphere–ocean system (dimensionless)
u	$-\cos\theta$ (dimensionless)
v_{eff}	Effective variance of hydrosol size distribution (dimensionless)
φ	Azimuth angle of the direction of light propagation, measured in the clockwise direction from the positive x axis when looking upwards (degrees)
W	Ocean surface wind speed ($\mathrm{m\ s}^{-1}$)
w_1, w_2	Weights of a two-term Henyey–Greenstein function (dimensionless)
ψ	Ocean surface wind direction (degrees)
ω_{blk}, ω_{aer}	Single scattering albedo for bulk oceanic water and aerosol particles, respectively (dimensionless)
$\mathbf{Z}$	Phase matrix of a volume element in the atmosphere–ocean system (4×4 matrix; dimensionless)

This research was funded by the NASA/Glory Mission project. The authors are also grateful for the insightful comments made by the late Glenn Cota on an earlier version of this manuscript, and by the anonymous reviewers of the submitted manuscript.

References

1. J. E. Hansen and L. D. Travis, "Light scattering in planetary atmospheres," Space Sci. Rev. **16,** 527– 610 (1974).
2. M. I. Mishchenko, L. D. Travis, and A. A. Lacis, *Scattering, Absorption, and Emission by Small Particles* (Cambridge U. Press, 2002).
3. M. I. Mishchenko and L. D. Travis, "Satellite retrieval of aerosol properties over the ocean using polarization as well as intensity of reflected sunlight," J. Geophys. Res. **102,** 16989–17013 (1997).
4. O. P. Hasekamp and J. Landgraf, "Retrieval of aerosol properties over the ocean from multispectral single-viewing-angle measurements of intensity and polarization: Retrieval approach, information content, and sensitivity study," J. Geophys. Res. **110,** D20207, doi:10.1029/2005JD006212 (2005).
5. J. Chowdhary, B. Cairns, M. I. Mishchenko, and L. D. Travis, "Retrieval of aerosol properties over the ocean using multispectral and multiangle photopolarimetric measurements from the Research Scanning Polarimeter," Geophys. Res. Lett. **28,** 243–246 (2001).
6. B. Gérard, J.-L. Deuzé, M. Herman, Y. J. Kaufman, P. Lallart, C. Oudard, L. A. Remer, B. Roger, B. Six, and D. Tanré, "Comparisons between POLDER 2 and MODIS/Terra aerosol retrievals over ocean," J. Geophys. Res. **110,** D24211, doi: 10.1029/2005JD006218 (2005).
7. H. R. Gordon, O. B. Brown, R. H. Evans, J. W. Brown, R. C. Smith, K. S. Baker, and D. K. Clark, "A semianalytical radiance model of ocean color," J. Geophys. Res. **93,** 10909–10924 (1988).
8. A. Morel, "Optical modeling of the upper ocean in relation to its biogenous matter content (case I waters)," J. Geophys. Res. **93,** 10749–10768 (1988).
9. H. R. Gordon, "Atmospheric correction of ocean color imagery in the Earth Observing System era," J. Geophys. Res. **102,** 17081–17106 (1997).
10. J. Chowdhary, B. Cairns, and L. D. Travis, "Case studies of aerosol retrievals over the ocean from multiangle, multispectral photopolarimetric remote sensing data," J. Atmos. Sci. **59,** 383–397 (2002).
11. B. Cairns, L. D. Travis, and E. E. Russel, "The Research Scanning Polarimeter: calibration and ground-based measurements," in *Polarization: Measurements, Analysis, and Remote Sensing II,* D. H. Goldstein and D. H. Chenault, eds., Proc. SPIE **3754,** 186–196 (1999).
12. M. I. Mishchenko, B. Cairns, J. E. Hansen, L. D. Travis, R. Burg, Y. J. Kaufman, J. V. Martins, and E. P. Shettle, "Monitoring of aerosol forcing of climate from space: analysis of measurement requirements," J. Quant. Spectrosc. Radiat. Transfer **88,** 149–161 (2004).
13. T. J. Petzold, "Volume scattering functions for selected ocean waters," in *Light in Sea,* J. E. Tyler, ed. (Dowden, Hutchinson, and Ross, 1977), pp. 152–157.
14. M. Chami, R. Santer, and E. Dillegeard, "Radiative transfer model for the computation of radiance and polarization in an atmosphere–ocean system: polarization properties of suspended matter for remote sensing," Appl. Opt. **40,** 2398–2416 (2001).
15. D. Stramski and D. A. Kiefer, "Light scattering by microorganisms in the open ocean," Prog. Oceanog. **28,** 343–381 (1991).
16. A. Morel and S. Maritorena, "Bio-optical properties of oceanic waters: a reappraisal," J. Geophys. Res. **106,** 7163–7180 (2001).
17. H. Volten, J. F. de Haan, J. W. Hovenier, R. Schreurs, W. Vassen, A. G. Dekker, H. J. Hoogenboom, and F. Charlton, "Laboratory measurements of angular distributions of light scattering by phytoplankton and silt," Limnol. Oceanogr. **43,** 1180–1197 (1998).
18. O. B. Brown and H. R. Gordon, "Two component Mie scattering models of Sargasso Sea particles," Appl. Opt. **12,** 2461–2465 (1973).
19. J. R. Zaneveld, D. M. Roach, and H. Pak, "The determination of the index of refraction distribution of oceanic particles," J. Geophys. Res. **79,** 4091–4095 (1974).
20. H. R. Gordon, "Diffuse reflectance of the ocean: influence of nonuniform phytoplankton pigment profile," Appl. Opt. **31,** 2116–2129 (1992).
21. O. Ulloa, S. Sathyendranath, and T. Platt, "Effect of the particle-size distribution on the backscattering ratio in seawater," Appl. Opt. **33,** 7070–7077 (1994).
22. M. S. Twardowski, E. Boss, J. B. Macdonald, W. S. Pegau, A. H. Bernard, and J. R. V. Zaneveld, "A model for estimating bulk refractive index from the optical backscattering efficiency ratio and the implications for understanding particle composition in case I and II waters," J. Geophys. Res. **106,** 14129–14142 (2001).
23. G. N. Plass and G. W. Kattawar, "Monte Carlo calculations of radiative transfer in the Earth's atmosphere–ocean system: I. Flux in the atmosphere and ocean," J. Phys. Oceanogr. **2,** 139–145 (1972).
24. M. Tanaka and T. Nakajima, "Effects of oceanic turbidity and

index of refraction of hydrosols on the flux of solar radiation in the atmosphere-ocean system," J. Quant. Spectrosc. Radiat. Transfer **18,** 93–111 (1977).
25. K. Masuda and T. Takashima, "Sensitivity of radiation absorbed in the ocean to atmospheric and oceanic parameters in the short wavelengths region. Part 1. Cloudless atmosphere," J. Meteorol. Soc. Japan **66,** 617–628 (1988).
26. G. W. Kattawar and G. N. Plass, "Radiative transfer in the Earth's atmosphere–ocean system: II. Radiance in the atmosphere and ocean," J. Phys. Oceanogr. **2,** 146–156 (1972).
27. J. Fischer and H. Grassl, "Radiative transfer in an atmosphere–ocean system: an azimuthal dependent matrix-operator approach," Appl. Opt. **23,** 1023–1039 (1984).
28. G. W. Kattawar, G. N. Plass, and J. A. Guinn, Jr., "Monte Carlo calculations of the polarization of radiation in the Earth's atmosphere–ocean system," J. Phys. Oceanogr. **3,** 353–372 (1973).
29. K. Masuda and T. Takashima, "Dependence of the radiation just above and below the ocean surface on atmospheric and oceanic parameters," Appl. Opt. **23,** 4891–4898 (1988).
30. D. Stramski and C. D. Mobley, "Effects of microbial particles on ocean optics: a database of single-particle optical properties," Limnol. Oceanogr. **42,** 538–549 (1997).
31. D. Stramski, A. Bricaud, and A. Morel, "Modeling the inherent optical properties of the ocean based on the detailed composition of the planktonic community," Appl. Opt. **40,** 2929–2945 (2001).
32. H. R. Gordon and G. C. Boynton, "Radiance–irradiance inversion algorithm for estimating the absorption and backscattering coefficients of natural waters: homogeneous water," Appl. Opt. **36,** 2636–2641 (1997).
33. H. Loisel, D. Stramski, B. G. Mitchel, F. Fell, V. Fournier-Sicre, B. Lemasle, and M. Babin, "Comparison of the ocean inherent properties obtained from measurements and inverse modeling," Appl. Opt. **40,** 2384–2397 (2001).
34. A. Morel and B. Gentilli, "Diffuse reflectance of oceanic waters: its dependence on sun angle as influenced by the molecular scattering contribution," Appl. Opt. **30,** 4427–4438 (1991).
35. A. Morel and B. Gentilli, "Diffuse reflectance of oceanic waters. II. Bidirectional aspects," Appl. Opt. **32,** 6864–6878 (1993).
36. A. Morel and B. Gentilli, "Diffuse reflectance of oceanic waters. III. Implication of bidirectionality for the remote-sensing problem," Appl. Opt. **35,** 4850–4862 (1996).
37. A. Morel and I. Prieur, "Analysis of variations in ocean color," Limnol. Oceanogr. **22,** 709–722 (1977).
38. V. I. Haltrin, "Chlorophyll-based model of seawater optical properties," Appl. Opt. **38,** 6826–6832 (1999).
39. V. I. Haltrin, "One-parameter two-term Henyey–Greenstein phase function for light scattering in seawater," Appl. Opt. **41,** 1022–1028 (2002).
40. C. D. Mobley, L. K. Sundman, and E. Boss, "Phase function effects on oceanic light fields," Appl. Opt. **41,** 1035–1050 (2002).
41. H. Mehrtens and T. Martin, "Remote sensing of oligotrophic waters: model divergence at low chlorophyll concentrations," Appl. Opt. **41,** 7058–7067 (2002).
42. A. Morel, D. Antoine, and B. Gentili, "Bidirectional reflectance of oceanic waters: Accounting for Raman emission and varying particle scattering phase function," Appl. Opt. **41,** 6289–6306 (2002).
43. J. W. Hovenier and C. V. M. van der Mee, "Fundamental relationships relevant to the transfer of polarized light in a scattering atmosphere," Astron. Astrophys. **128,** 1–16 (1983).
44. M. I. Mishchenko, "Vector radiative transfer equation for arbitrary shaped and arbitrary oriented particles: a microphysical derivation from statistical electromagnetics," Appl. Opt. **41,** 7114–7134 (2002).
45. M. I. Mishchenko, D. W. Mackowski, and L. D. Travis, "Scattering of light by bispheres with touching and separated components," Appl. Opt. **34,** 4589–4599 (1995).
46. H. C. van de Hulst, *Light Scattering by Small Particles* (Wiley, 1957).
47. H. R. Gordon, "Modeling and simulating radiative transfer in the ocean," in *Ocean Optics,* R. W. Spinrad, K. L. Carder, M. J. Perry, eds. (Oxford U. Press, 1994).
48. H. R. Gordon and A. Morel, *Remote Assessment of Ocean Color for Interpretation of Satellite Visible Imagery: A Review* (Springer-Verlag, 1983).
49. A. Bricaud, A. Morel, M. Babin, K. Allali, and H. Claustre, "Variations of light absorption by suspended particles with chlorophyll a concentration in oceanic (case 1) waters: analysis and implications for bio-optical models," J. Geophys. Res. **103,** 31033–31044 (1998).
50. A. Bricaud, A. Morel, M. Babin, K. Allali, H. Claustre, Erratum: "Variations of light absorption by suspended particles with chlorophyll a concentration in oceanic (case 1) waters: analysis and implications for bio-optical models," J. Geophys. Res. **104,** 8025 (1999).
51. L. Prieur and S. Sathyendranath, "An optical classification of coastal and oceanic waters based on the specific spectral absorption curves of phytoplankton pigments, dissolved organic matter, and other particulate matter," Limnol. Oceanogr. **26,** 671–689 (1981).
52. R. C. Smith, and K. S. Baker, "Optical properties of the clearest natural waters (200–800 nm)," Appl. Opt. **20,** 177–184 (1981).
53. R. M. Pope and E. S. Fry, "Absorption spectrum (380–700 nm) of pure water. II. Integration cavity measurements," Appl. Opt. **36,** 8710–8723 (1997).
54. A. Morel, "Optical properties of pure water and pure sea water," in *Optical Aspects of Oceanography,* N. G. Jerlov and E. Steeman Nielsen, eds. (Academic Press, 1974), pp. 1–24.
55. D. Stramski, E. Boss, D. Bogucki, and K. J. Voss, "The role of seawater constituents in light backscattering in the ocean," Prog. Oceanog. **61,** 27–56 (2004).
56. M. Jonasz, "Nonsphericity of suspended marine particles and its influence on light scattering," Limnol. Oceanogr. **32,** 1059–1065 (1987).
57. M. S. Quinby-Hunt, A. J. Hunt, K. Lofftus, and D. Shapiro, "Polarized-light scattering studies of marine Chlorella," Limnol. Oceanogr. **34,** 1587–1600 (1989).
58. J. C. Kitchen and J. R. V. Zaneveld, "A three-layered sphere model of optical properties of phytoplankton," Limnol. Oceanogr. **37,** 1680–1690 (1992).
59. M. I. Mishchenko, J. W. Hovenier, and L. D. Travis, *Light Scattering by Non-Spherical Particles* (Academic Press, 2000).
60. A. Quirantes and S. Benard, "Light scattering by marine algae: two-layer spherical and nonspherical models," J. Quant. Spectrosc. Radiat. Transfer **89,** 311–321 (2004).
61. K. J. Voss and E. S. Fry, "Measurement of the Mueller matrix for ocean water," Appl. Opt. **23,** 4427– 4439 (1984).
62. E. S. Fry and K. J. Voss, "Measurement of the Mueller matrix for phytoplankton," Limnol. Oceanogr. **30,** 1322–1326 (1985).
63. A. Kouzoubov, M. J. Brennan, and J. C. Thomas, "Treatment of polarization in laser remote sensing," Appl. Opt. **37,** 3873–3885 (1998).
64. H. R. Gordon, "Diffuse reflectance of the ocean: the theory of its augmentation by chlorophyll a fluorescence at 685 nm," Appl. Opt. **18,** 1161–1166 (1979).
65. D. Spitzer and R. W. J. Dirk, "Contamination of the reflectance of natural waters by solar-induced fluorescence of dissolved organic matter," Appl. Opt. **24,** 444–445 (1985).
66. H. R. Gordon, "Contribution of Raman scattering to water-leaving radiance: a reexamination," Appl. Opt. **38,** 3166–3174 (1999).
67. R. W. Spinrad and J. F. Brown, "Relative real refractive index

of marine microorganisms: a technique for flow cytometric estimation," Appl. Opt. **25,** 1930–1934 (1986).
68. E. Aas, "Refractive index of phytoplankton derived from its metabolite composition," J. Plankton. Res. **18,** 2223–2249 (1996).
69. S. Woźniak and D. Stramski, "Modeling the optical properties of mineral particles suspended in seawater and their influence on ocean reflectance and chlorophyll estimation from remote sensing algorithms," Appl. Opt. **43,** 3489–3503 (2004).
70. M. Jonasz and H. Prandke, "Comparison of measured and computed light scattering in the Baltic," Tellus, Ser. B **38B,** 144–157 (1986).
71. M. Jonasz, "Particle-size distributions in the Baltic," Tellus, Ser. B **35,** 346–35 (1983).
72. D. Risović, "Two-component model of sea particle size distribution," Deep-Sea Res. I **40,** 1459–1473 (1993).
73. D. Risović, "Effect of suspended particulate-size distribution on the backscattering ratio in the remote sensing of seawater," Appl. Opt. **41,** 7092–7100 (2002).
74. Y. A. Kad'shevich and Y. S. Lyubovtseva, "Certain characteristics of ocean hydrosols from scattering matrices," Izv., Acad. Sci., USSR, Atmos. Oceanic. Phys. **9,** 659–663 (1973).
75. T. Takashima, "Polarization effect on radiative transfer in planetary atmospheres with interacting surfaces," Earth, Moon, Planets **33,** 59–97 (1985).
76. J. F. de Haan, P. B. Bosma, and J. W. Hovenier, "The adding method for multiple scattering computations of polarized light," Astron. Astrophys. **183,** 371–391 (1987).
77. J. Chowdhary, "Multiple scattering of polarized light in atmosphere-ocean systems", Ph.D. thesis (Columbia University, New York, 1999).
78. W. A. de Rooij and C. C. A. H. van der Stap, "Expansion of Mie scattering matrices in generalized spherical functions," Astron. Astrophys. **131,** 237–248 (1984).
79. H. Loisel and A. Morel, "Light scattering and chlorophyll concentration in case 1 waters: a reexamination," Limnol. Oceanogr. **43,** 847–858 (1998).
80. H. R. Gordon and W. R. McCluney, "Estimation of the depth of sunlight penetration in the sea for remote sensing," Appl. Opt. **14,** 413–416 (1975).
81. M. Stramska and D. Stramski, "Effects of a nonuniform profile of chlorophyll concentration on remote-sensing reflectance of the ocean," Appl. Opt. **44,** 1735–1747 (2005).
82. J. Chowdhary, B. Cairns, M. I. Mishchenko, P. V. Hobbs, G. F. Cota, J. Redemann, K. Rutledge, B. N. Holben, and E. Russel, "Retrievals of aerosol scattering and absorption properties from photo-polarimetric observations over the ocean during the CLAMS experiment," J. Atmos. Sci. **62,** 1093–1117 (2005).
83. C. Cox and W. Munk, "Statistics of the sea-surface derived from sun-glitter," J. Mar. Res. **13,** 198–227 (1954).
84. M. I. Sancer, "Shadow-corrected electromagnetic scattering from a randomly-rough ocean surface," IEEE Trans. Antennas Propag. **17,** 557–585 (1969).
85. P. Koepke, "Effective reflectance of oceanic whitecaps," Appl. Opt. **23,** 1816–1842 (1984).
86. R. Frouin, M. Schindling, and P.-Y. Deschamps, "Spectral reflectance of sea-foam in the visible and near-infrared: In-situ measurements and remote sensing applications," J. Geophys. Res. **101,** 14361–14371 (1996).
87. R. W. Preisendorfer and C. D. Mobley, "Albedos and glitter patterns of a wind-roughened sea surface," J. Phys. Oceanogr. **16,** 1293–1316 (1986).
88. J. E. Hansen, "Multiple scattering of polarized light in planetary atmospheres. Part II. Sunlight reflected by terrestrial clouds," J. Atmos. Sci. **28,** 1400–1426 (1971).
89. R. E. Walker, *Marine Light Field Statistics* (Wiley, 1994).
90. H. R. Gordon, "Normalized water-leaving radiance: revisiting the influence of surface roughness," Appl. Opt. **44,** 241–248 (2005).
91. P. Stamnes, J. F. de Haan, and J. W. Hovenier, "The polarized internal radiation field of a planetary atmosphere," Astron. Astrophys. **225,** 239–259 (1989).
92. J. W. Hovenier, "Symmetry relationships for scattering of polarized light in a slab of randomly oriented particles," J. Atmos. Sci. **26,** 488–499 (1969).
93. Z. Jin, T. P. Charlock, and K. Rutledge, "Analysis of broadband solar radiation and albedo over the ocean surface at COVE," J. Atmos. Ocean. Technol. **19,** 1585–1601 (2002).
94. J. W. Hovenier and J. F. de Haan, "Polarized light in planetary atmospheres for perpendicular directions," Astron. Astrophys. **146,** 185–191 (1985).
95. J. T. Adams, E. Aas, N. K. Højerslev, and B. Lundgren, "Comparison of radiance and polarization values observed in the Mediterranean Sea and simulated in a Monte Carlo model," Appl. Opt. **41,** 2724–2733 (2002).
96. G. W. Kattawar, "A three-parameter analytical phase function for multiple scattering calculations," J. Quant. Spectros. Radiat. Transfer **15,** 839–849 (1975).
97. M. E. Lee and M. R. Lewis, "A new method for the measurement of the optical volume scattering function in the upper ocean," J. Atmos. Ocean. Technol. **20,** 563–571 (2003).
98. G. Kullenberg, "Observations of light scattering in two oceanic areas," Deep-Sea Res. **31,** 295–316 (1984).
99. A. Morel and H. Loisel, "Apparent optical properties of oceanic water: dependence on the molecular scattering contribution," Appl. Opt. **21,** 4765–4776 (1998).
100. M. Born and E. Wolf, *Principles of Optics* (Pergamon, 1980).
101. G. W. Kattawar, and C. N. Adams, "Stokes vector calculations of the submarine light field in an atmosphere-ocean with scattering according to a Rayleigh phase matrix: effect of interface refractive index on radiance and polarization," Limnol. Oceanogr. **34,** 1453–1472 (1989).
102. D. Stramski and S. B. Woźniak, "On the role of colloidal particles in light scattering in the ocean," Limnol. Oceanogr. **50,** 1581–1591 (2005).